Astronomy & Astrophysics manuscript no. hydroBetaPlane
March 11, 2016
© ESO 2016

Shear–driven instabilities and shocks in the atmospheres of hot Jupiters

Sébastien Fromang[1,2], Jeremy Leconte[3,4] and Kevin Heng[5]

[1] Laboratoire AIM, CEA/DSM-CNRS-Université Paris 7, Irfu/Service d'Astrophysique, CEA-Saclay, 91191 Gif-sur-Yvette, France
[2] Institut dAstrophysique de Paris and UPMC, CNRS (UMR 7095) , 98 bis Boulevard Arago, 75014, Paris, France
[3] Univ. Bordeaux, LAB, UMR 5804, F-33270, Floirac, France
[4] CNRS, LAB, UMR 5804, F-33270, Floirac, France
[5] University of Bern, Center for Space and Habitability, Sidlerstrasse 5, CH-3012, Bern, Switzerland
e-mail: sebastien.fromang@cea.fr

Accepted; Received; in original form;

arXiv:1603.02794v2 [astro-ph.EP] 10 Mar 2016

ABSTRACT

Context. General circulation models of the atmosphere of hot Jupiter have shown the existence of a supersonic eastward equatorial jet. Yet these results have been obtained using numerical schemes that filter out vertically propagating sound waves and assume vertical hydrostatic equilibrium, or with fully compressive codes that use large dissipative coefficients.
Aims. In this paper, we remove both limitations and investigate the effects of compressibility on the atmospheric dynamics by solving the standard Euler equations.
Methods. This is done by means of a series of simulations performed in the framework of the equatorial β–plane approximation using the finite volume shock–capturing code RAMSES.
Results. At low resolution, we recover the classical results described in the literature: we find a strong and steady supersonic equatorial jet of a few km.s^{-1} that displays no signature of shocks. We next show that the jet zonal velocity depends significantly on the grid meridional resolution. When that resolution is fine enough to properly resolve the jet, the latter is subject to a Kelvin-Helmholtz instability. The jet zonal mean velocity displays regular oscillations with a typical timescale of few days and a significant amplitude of about 15% of the jet velocity. We also find compelling evidence for the development of a vertical shear instability at pressure levels of a few bars. It seems to be responsible for an increased downward kinetic energy flux, significantly affecting the temperature of the deep atmosphere, and appears to act as a form of drag on the equatorial jet. This instability also creates velocity fluctuations that propagate upward and steepen into weak shocks at pressure levels of a few mbars.
Conclusions. We conclude that hot Jupiter equatorial jets are potentially unstable to both a barotropic Kelvin-Helmholtz instability and a vertical shear instability. Upon confirmation using more realistic models, both instabilities could result in significant time variability of the atmospheric winds, may provide a small scale dissipation mechanism in the flow, and might have consequences for the internal evolution of hot Jupiters.

1. Introduction

In the last decade, hot Jupiters observations have evolved from characterizing only the orbital (semi major axis, period, eccentricity) and structural (mass and radius) properties of the newly discovered planets to constraining also the physical properties of the atmosphere such as the composition and the temperature–pressure profile (Madhusudhan et al. 2014; Heng & Showman 2015), as well as observables that are directly connected to the dynamics such as 2D brightness maps (Knutson et al. 2007; de Wit et al. 2012) and even (although maybe still tentatively) atmospheric winds (Snellen et al. 2010). With new instruments such as the James Webb Space Telescope (JWST) soon available to the community, future observations will become more and more constraining. Their interpretation and understanding will require elaborate and well understood models of the dynamical structure of their upper atmosphere. Such a need explains the recent development by several groups of numerical models describing the atmospheric dynamics of hot Jupiters (among which Showman & Guillot 2002; Menou et al. 2003; Cho et al. 2008; Showman et al. 2008, 2009; Dobbs-Dixon & Lin 2008; Rauscher & Menou 2010; Heng et al. 2011b), a comprehensive review of which has recently been published by Heng & Showman (2015). Taken as a whole, these global circulation models (GCM) have produced a few robust results that characterize the dynamics of hot Jupiter atmospheres. Probably the most notable is the existence of an equatorial jet with typical eastward gas velocity of the order of a few kilometers per second as first shown by Showman & Guillot (2002). This is faster than the speed of sound by a factor of a few (i.e. the Mach number of the jet, defined as the ratio between the wind and the sound speed, is larger than unity). This remarkable result comes from the fact that hot Jupiters are both tidally locked and strongly irradiated by their central star as a result of the small semi major axis of their orbit. It has been given theoretical grounds by the semi–analytical calculations of Showman & Polvani (2010, 2011) who could explain the origin of the equatorial jet by the excitation of a stationary planetary scale Rossby wave by stellar irradiation, a result recently confirmed and extended to include three dimensional effects by Tsai et al. (2014). One reason of the success of these models is that they appear to be consistent with some of the observations of hot Jupiter atmospheres, such as the eastward shift of the hot spot at

Send offprint requests to: s.fromang

the photosphere (Knutson et al. 2007) or the day–night temperature contrast measurements (Perez-Becker & Showman 2013).

Despite these significant findings, several questions remain. First, the supersonic nature of the equatorial jet have raised the question of the existence of shocks in hot Jupiters atmospheres. The presence of such structures could have important consequences for the atmosphere time variability and act as an efficient drag mechanism on the flow (Rauscher & Menou 2012). This question is made even more accute because many of the published results have been obtained using approaches borrowed from the community studying the earth atmosphere climate and use approximations that are well adapted to study the earth atmospheric dynamics. The most widely used is based on solving a reduced set of equations, the so–called primitive formulation of the hydrodynamics equations, that filters out vertically propagating sound waves and assumes that the gas is in hydrostatic equilibrium in the vertical direction. Such codes are only able to capture hydraulic jumps as opposed to real shocks (see Rauscher & Menou 2012, for a discussion of this issue). Using such approaches, several groups have reported the existence of regions where significant compression occurs and take the form of standing discontinuities (Showman et al. 2009; Rauscher & Menou 2010), suggesting that shocks might indeed develop, in agreement with theoretical arguments such as given by Heng (2012). In addition to these models, a few papers have been published and present simulations that do not rely of these standard GCM approximations and thus do not suffer from these limitations (Dobbs-Dixon & Lin 2008; Dobbs-Dixon et al. 2010; Mayne et al. 2014a,b). These groups solved the Navier-Stokes equations on the sphere and explicitly include some form of dissipation to stabilize the scheme and/or to account for the effect of unresolved features of the flow. Even though the issue of shocks is not the main focus of either of these papers, Dobbs-Dixon et al. (2010) report shock–like features in some of their models. However, the use of high dissipation coefficients in these particular simulations significantly changes the mean flow so that the issue of shocks formation in hot Jupiter atmospheres remains open.

In addition, it is possible that the equatorial jet is destabilized by various hydrodynamic instabilities. For example, Li & Goodman (2010) have recently shown using analytical arguments coupled with idealized numerical simulations that fast supersonic equatorial jets are vulnerable to a vertical shear instability, a possibility first mentionned by Showman & Guillot (2002)[1]. As shown by Li & Goodman (2010), shocks might develop during its nonlinear evolution and have significant consequences for the jet mean velocity. As explained by Li & Goodman (2010), properly resolving this instability in a GCM is a tremendous task because it requires that the numerical grid is sufficiently fine to resolve the vertical pressure scale height of the atmosphere *in the horizontal direction*. Given these difficulties and because of the very idealized nature of the numerical setup used by Li & Goodman (2010), it is perhaps not surprising that the question of the possible development and potential consequences of a vertical shear instability in hot Jupiter atmospheres has never been addressed in any GCM so far.

In addition to their importance as possible drag mechanisms, the questions of the existence of shocks and/or of the growth of hydrodynamic instabilities such as described above may have some potential observational consequences in terms of the flow variability, but also to explain the origin of the inflated hot Jupiters (Baraffe et al. 2010). Indeed, it has been suggested that downward transport of kinetic energy possibly associated with these instabilities (Showman & Guillot 2002; Guillot & Showman 2002) along with turbulent mixing of heat (Youdin & Mitchell 2010) might transport and deposit sufficient amount of thermal energy in the deep layers of the atmosphere to account for such highly inflated radii (for a detailed discussion, see Ginzburg & Sari 2015).

The purpose of this paper is to develop an idealized model in order to investigate the issues described above. For that purpose, we will solve the compressible Euler equations. Since we are interested in shocks, we will use the finite volume shock capturing scheme RAMSES (Teyssier 2002) that is based on the Godunov method (Toro 1997, see also section 2.3). In addition to being well adapted to resolving shocks in supersonic flows such as encountered here, finite volume code like RAMSES conserve the gas total energy, the sum of its kinetic and thermal energy, even in the absence of explicit dissipation. This means in particular that all the kinetic energy that might be numerically dissipated (as would be the case, for example, in a turbulent flow) goes back into heat. As noted by Goodman (2009), this is of particular importance in the context of hot Jupiter atmospheres. Our strategy in this first paper is to keep the numerical setup as simple as possible while retaining the basics ingredients that drive the flow dynamics. We will thus make two important simplifications regarding the thermodynamics and the geometry. While most published results now use a complex but realistic treatment of radiative transfer effects, we will model these effects with a simple parametrized cooling function. For practical purpose, we will use a form of the cooling function that is linear in the temperature, also known as Newtonian cooling. This has proved very useful in modelling atmospheric flows in general and hot Jupiter general circulation in particular (Showman et al. 2008; Rauscher & Menou 2010; Heng et al. 2011b). Published simulations using that approximation compares well with more realistic models that include a detailed treatment of radiative transfer effects (Dobbs-Dixon & Lin 2008; Showman et al. 2009; Heng et al. 2011a; Rauscher & Menou 2012). Our second approximation will be to solve the equations in a Cartesian geometry using the equatorial beta plane model. This is a well–known approximation in atmospheric dynamics and one that been successfully used recently in the context of hot Jupiter atmospheric flow (Showman & Polvani 2010, 2011; Tsai et al. 2014; Heng & Workman 2014). The idea is to focus on the equatorial region of the planet and to expand the vertical projection of its angular velocity linearly to the first order in the distance y to the equator:

$$\mathbf{\Omega} = \frac{1}{2}\beta y \boldsymbol{e}_z \,, \tag{1}$$

where β is a constant and a free parameter of the model, while $\boldsymbol{e}_z$ stands for the unit vector in the vertical direction. For hot Jupiter atmospheres, this is a particularly useful approximation because of their slow rotation and since the dynamics develops mainly at the vicinity of the equator. Using these simplifications but including the effect of compressibility, the goal of this paper is to investigate such questions as the occurrence of shocks, the stability of the equatorial jet and the origin of the flow variability, if any.

The plan of the paper is as follows. In section 2, we detail our numerical setup and the parameters we use. The idea is to use a set of numerical parameters as close as possible to the benchmark models presented by Heng et al. (2011b) and to investigate the potential effects induced by compressibility in this model. In

[1] It is worth reminding that such a vertical shear instability is by definition absent in any simulation that rely on the standard primitive formulation of hydrodynamics.

section 3, we present a low resolution model and show that we recover many of the features described in the literature despite our simplistic geometry. These results validate our approach and our approximations. In section 4, we make a quick resolution study before presenting a high resolution simulation in section 5. As we shall see, the flow features variability at different spatial and temporal scales that we relate to well known hydrodynamics instabilities. We then conclude and discuss the limitations of our work and the perspectives it opens in section 6.

2. Physical model and numerical implementation

2.1. Equations and notations

As explained in the introduction, we solve the hydrodynamic equations in a Cartesian coordinate system denoted by $(\boldsymbol{e_x}, \boldsymbol{e_y}, \boldsymbol{e_z})$, in a frame rotating with angular velocity $\boldsymbol{\Omega}$. We consider a grid that extends over the ranges $[-L_x/2, L_x/2]$, $[-L_y/2, L_y/2]$ and $[0, L_z]$ in the x, y and z directions, respectively. The x–direction should be thought of as representing longitudes in traditional GCM models, y as a proxy for latitudes and z would stand for the radial direction (aligned with the gravitational acceleration). Since hydrostatic equilibrium is not built into the equations, we do not use pressure coordinates in the vertical direction as is common in atmospheric sciences when solving the primitive formulation of hydrodynamics. The time evolution for the gas density ρ, the velocity $\boldsymbol{v}$ and the total energy E writes:

$$\frac{\partial \rho}{\partial t} + \boldsymbol{\nabla\cdot}(\rho \boldsymbol{v}) = 0\,, \tag{2}$$

$$\frac{\partial \rho \boldsymbol{v}}{\partial t} + \boldsymbol{\nabla\cdot}(\rho \boldsymbol{v}\boldsymbol{v} + P) = -\rho g \boldsymbol{e_z} - 2\rho \boldsymbol{\Omega}\boldsymbol{\times}\boldsymbol{v}\,, \tag{3}$$

$$\frac{\partial E}{\partial t} + \boldsymbol{\nabla\cdot}\left[(E + P)\boldsymbol{v}\right] = \mathcal{L}\,. \tag{4}$$

where g is the constant vertical acceleration due to the planet gravitational field, $\mathcal{L}$ is the cooling function (see section 2.2) and P denotes thermal pressure. It is related to the total energy with the relation:

$$E = \frac{1}{2}\rho \boldsymbol{v}^2 + \rho e = \frac{1}{2}\rho \boldsymbol{v}^2 + \frac{P}{\gamma - 1}\,. \tag{5}$$

In the above equation, we have introduced the adiabatic exponent of the gas γ and have assumed an ideal equation of state in writing the internal energy e as a function of thermal pressure. In that case, P also relates directly to the gas temperature T through the following equation:

$$P = \frac{\rho k T}{\mu m_H} = \rho \mathcal{R} T\,. \tag{6}$$

Here k is the Boltzmann constant, μ is the mean molecular weight, m_H the mass of the hydrogen atom and $\mathcal{R}$ is the specific gas constant. Throughout this paper, we will assume the atmosphere is composed of a mixture of hydrogen and helium and we will take for $\mathcal{R}$ the same numerical value as Heng et al. (2011b): $\mathcal{R} = 3779$ J.kg^{-1}.m^{-1}. We will also set $\gamma = 1.4$. Finally, as explained in the introduction, we work in the framework of the equatorial β–plane model, so that $\boldsymbol{\Omega}$ is given by Eq. (1). In the remainder of this paper, we will thus refer to the $y = 0$ plane as "the equator".

2.2. The cooling function $\mathcal{L}$

$\mathcal{L}$ varies linearly with the departure from an equilibrium temperature, a prescription that is also known as Newtonian cooling:

$$\mathcal{L} = \frac{\rho \mathcal{R}}{\gamma - 1}\frac{T - T_{eq}}{\tau_{rad}}\,, \tag{7}$$

where T_{eq} and τ_{rad} are the radiative equilibrium temperature and radiative cooling timescale, respectively. They both depend a priori on the location in the atmosphere. $\mathcal{L}$ is meant to provide a rough but computationally straightforward description of the balance between heating due to stellar irradiation and radiative cooling. Our choice for the spatial dependence of τ_{rad} is discussed in section 2.4 and appendix A. To calculate T_{eq}, we followed a procedure that is largely inspired by (but not identical to, essentially because we use a different coordinate system) the benchmark calculation presented by Heng et al. (2011b). We describe it here briefly for completeness. We started from a reference pressure–dependent temperature profile T_P^0 that is usually computed from 1D radiative transfer calculations. We next defined:

$$T_{\rm day/night} = T_P^0 \pm \Delta T\,, \tag{8}$$

where ΔT is a constant and a free parameter of the simulation. For simplicity, we did not prescribe any pressure variation for ΔT, which is different from papers published in the literature that use Newtonian cooling to model radiative effects. Because the planet is tidally locked, the substellar point is fixed in time. We chose its horizontal coordinates to be $(x, y) = (0, 0)$. Using these definitions for T_{day} and T_{night}, we calculated T_{eq} as follows: on the night side of the planet ($|x| > L_x/4$), we followed Heng et al. (2011b) and set $T_{eq} = T_{\rm night}$. On the planet day side ($|x| < L_x/4$), we used the relation:

$$T_{eq}^4 = T_{night}^4 + (T_{day}^4 - T_{night}^4)\cos\left(\frac{2\pi x}{L_x}\right)\exp\left(-\frac{y^2}{2L_{th}^2}\right)\,. \tag{9}$$

Note that this profile is different from the functional form of T_{eq} introduced by Heng et al. (2011b). While the sinusoidal x–dependence is reminiscent of their longitudinal profile, a similar dependence would have little meaning in the y–direction. It is more natural to use an exponential variation in that direction, as done recently by Showman & Polvani (2011). The drawback of this formulation is that it introduces an additional length scale L_{th} in the problem that is another free parameter of the model. The specific value we chose in this paper is discussed below in section 2.4.

2.3. Numerical implementation

We solve the above equations using a uniform grid version of the community code RAMSES (Teyssier 2002). RAMSES uses a finite volume scheme based on the MUSCL-Hancock Godunov method (Toro 1997). By systematically upwinding all the waves that enter in the problem, finite volume codes are intrinsically stable (provided they satisfy the Courant–Friedrich–Lax, or CFL, condition) and do not require using any explicit dissipation. In fact, the algorithm is constructed to add the minimum amount of dissipation that is necessary to stabilize the numerical scheme. This is important for one of the problems we are interested in, namely the issue of shock formation. However, a well–known difficulty of Godunov codes is their inability to properly handle vertical hydrostatic equilibrium (see,

e.g. LeVeque 1998). This is because the latter results from a balance between two terms that are treated differently by the numerical algorithm, namely the pressure gradient (treated as a flux of momentum computed as part of the solution of a Riemann problem) and gravity (treated as a source term by a simple split Crank-Nicholson algorithm). Starting from a solution initially in exact equilibrium balance, this situation immediately creates a mass flux at cell interfaces that rapidly leads to spurious vertical velocities (even in 1D) and compromises the simulation. Recently, Käppeli & Mishra (2014) developed an algorithm for the MUSCL–Hancock scheme that is especially designed to fix that problem. The idea is to suppose that the density and pressure profiles within each cells are isentropic, and to use the extrapolated values at cell faces as inputs for the Riemann problem. We have implemented their solution in RAMSES and found that it gives very satisfactory results, in the sense that the code is now able to keep a stratified atmosphere in hydrostatic equilibrium with almost vanishing deviations.

The boundary conditions (BC) we used are periodic in the x–direction. Because the Coriolis force increases in amplitude with y, the dynamics is confined to the vicinity of the equator. For this reason, the boundary conditions in the y–direction are not critical provided the domain is chosen wide enough. In the simulations presented in this paper, we set the horizontal velocity to zero there and assumed zero–gradient for all other variables. The vertical boundary conditions are more subtle to implement and somewhat arbitrary. We empirically found that the following produces good results, in the sense that artifacts introduced by the boundaries could not be detected: we extrapolated both density and pressure assuming an isentropic vertical profile, imposed zero gradient horizontal velocity gradient and reflective BC on the vertical momentum. In addition, we forced the mass, momentum and energy fluxes to vanishes at the vertical boundaries. We note that the two conditions (on the variables themselves and on the fluxes) are not necessarily consistent with each other, but did not lead to any problem in the simulations.

The numerical implementation described above was tested by reproducing standard results of the literature. We present two of them in the appendix of the paper, namely the growth of a baroclinic wave in an adiabatic atmosphere as described by Polichtchouk et al. (2014) in appendix B.1 and a shallow hot Jupiter model such as presented by Menou & Rauscher (2009); Heng et al. (2011b); Mayne et al. (2014a) in appendix B.2. Although these tests do not have an analytical solution, the similarity between our results and the published calculations, along with the analysis of a low resolution deep model that we present in section 3 give confidence in our setup.

2.4. Model parameters

The physical model presented above contains several free parameters: g and β characterize the planet, while T_P^0, τ_{rad}, ΔT and L_{th} describes the heating and cooling processes. Rather than presenting a complete survey of the associated parameter space, the idea of the present paper is to choose a unique set of parameters that matches as closely as possible those of Heng et al. (2011b) and to show that the flow properties are similar to the results presented in that paper. We defer a detailed study of the influence of these free parameters on the results to a future publication.

Planet parameters: we follow the shallow hot Jupiter model of Heng et al. (2011b) and consider a planet with a radius $a_p = 10^8$ meters (m) and for which $g = 8$ m.s^{-2}. We assume the planet rotates with a frequency $\Omega_p = 2.1 \times 10^{-5}$ s^{-1}. Expanding $\Omega = \Omega_p \sin(\phi)$, where ϕ is the latitude, close to the equator, and using Eq. (1), we thus have:

$$\beta = \frac{2\Omega_p}{a_p} = 4.2 \times 10^{-13} \text{ m}^{-1}.\text{s}^{-1} . \quad (10)$$

Newtonian cooling parameters: we next need to prescribe the parameters entering in the definition of T_{eq} and τ_{rad}. To do so, we use an analytic relationship between T_P^0 and P, as well as between τ_{rad} and pressure. Both functions are given in appendix A and have numerical parameters chosen to give an approximate match to the profiles of Heng et al. (2011b). We also set $\Delta T = 300$ K in all our simulations. The curves so obtained for T_{night} and T_{day} are plotted on figure A.1 and are close to the profiles used by Heng et al. (2011b, see their figure 7). It is worth noting that τ_{rad} becomes infinite below 10 bars. This choice creates an "inert layer" at location where $P > 10$ bars, in the sense that gas cannot cool radiatively in that region. As we shall see, this point turned out to have rather important consequences in the simulations. Finally, the cooling function $\mathcal{L}$ depends on the parameters L_{th} that governs its y–dependence. Apart from being of order a_p, there is no obvious way of choosing L_{th} and its influence on the flow properties deserves further investigations. After a few tests at low resolution, we found a good agreement with published results for $L_{th} = 0.7a_p$. We will use this value in the remainder of the paper.

Computational domain and initial conditions: we need to specify the extend of the computational domain and the initial conditions. We used $L_x = 2\pi a_p$ in the x direction and found that $L_y = 2.5a_p$ was wide enough for the lateral boundaries to have no effect on the flow topology. As noted by Mayne et al. (2014a), the vertical extent of the box has to be chosen carefully, because hot gas of the planet day side is inflated and expands upward. We thus followed these authors and used $L_z = 9 \times 10^6$ meters. Except for one model (see section 5), our calculations were all initiated from an atmosphere at rest ($\boldsymbol{v} = \boldsymbol{0}$ everywhere), with a uniform temperature $T = 1800$ K and in vertical hydrostatic equilibrium. We set the density in the bottom layer (i.e. at $z = 0$) so that $P = 220$ bars. With these parameters, we typically found that the pressure at the top of the domain ranges between 6×10^{-3} and 0.1 mbars, i.e. well below the typical pressures we will be interested in in the remainder of the paper. We note that there is a current debate in the literature regarding the sensitivity of the flow to the initial conditions (Thrastarson & Cho 2010; Liu & Showman 2013), particularly when explicit dissipation is small or vanishing as we consider here (Cho et al. 2015). Here, we leave these questions aside and consider the same initial conditions as used by Heng et al. (2011b).

Simulation post treatment: Unless otherwise stated, we typically produce snapshots of all the physical variables every planet day during the simulation. To ease comparison with published papers, we present all of our results interpolated in the vertical direction on a pressure grid that extends from 200 bars at the bottom to 1 mbars at the top using 48 levels uniformly spaced in the logarithm of the pressure.

Finally, we measure time in unit of one planet day, which corresponds to 299200 seconds with our choice of parameters, or about 3.5 Earth days. In the simulations we present below,

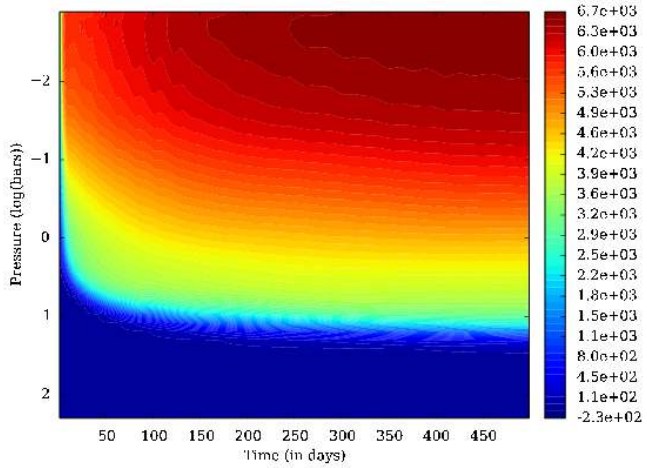

Fig. 2: Spacetime diagram (i.e time evolution of the pressure profile) of the zonally averaged zonal wind at the equator in the low resolution model.

the timestep is always limited by sound waves propagating in the vertical direction. It is typically of the order of 25 seconds in model LowRes (section 3) and 15 seconds in model HighRes (section 5). This should be contrasted with the typical timesteps of 120 seconds used by, for example, Heng et al. (2011b). Although markedly larger when using the primitive set of hydrodynamics equations, the difference with a fully compressible set of equations is not large enough to be prohibitive when performing hot Jupiter atmosphere simulations. This is because the typical pressure scale height H is large in this case (typically 10^3 km) so that the ratio between H and the horizontal scales involved in the problem is not as small as it would be for an Earth–like simulation.

3. Low resolution model

In order to validate our numerical implementation and our choice for the numerical parameters entering in the problem, we start by presenting a low resolution model (labelled LowRes in the following). The grid spatial resolution is set to $(N_x, N_y, N_z) = (64, 33, 48)$ in this section. This is smaller by about a factor of two than the resolution used by the finite difference core of Heng et al. (2011b). However, we did not used any explicit dissipation here, so that a one to one correspondence is difficult to establish a priori. The model was integrated for 500 planet days, which corresponds to about 1700 earth days for our choice of Ω_p.

We now describe the climatology of the atmosphere. As previously documented in the literature, the flow develops a strong eastward jet around the planet equator (figure 1, left panel). In about 200 days, it reaches a steady state at pressure level above 1 bar, while larger pressure levels gradually accelerate until the end of the simulation (figure 2). Based on this result, we computed the mean properties of the flow by calculating time averages from $t = 200$ until the end of the simulation. The zonally averaged jet velocity at the equator reaches about 6.6 km.s^{-1} at the top of the atmosphere (i.e. at a pressure level of about 1 mbar), which corresponds to a mean Mach number of about 2. As a result of the short radiative timescale in the atmosphere (compared to the dynamical timescale), the temperature structure displays a structure that is close to the zonally averaged

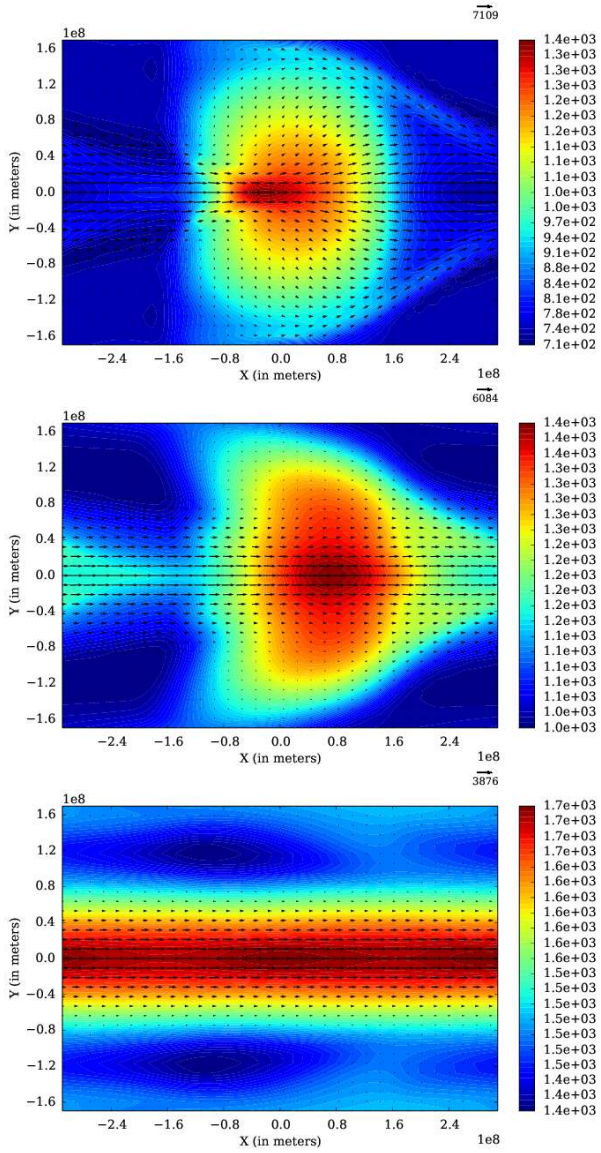

Fig. 3: Time averaged temperature (color contour) and horizontal wind (arrows) for the low resolution model at pressure level $P = 1.66$ mbars (*top panel*), $P = 97$ mbars (*middle panel*) and $P = 4.4$ bars (*bottom panel*). The time average is performed from $t = 200$ days to $t = 500$ days using 300 snapshots.

radiative equilibrium temperature, except in the deep layers of the atmosphere (at $P = 10$ bars and below) where a hot spot is seen with T up to 2000 K. We find very little velocity fluctuations in the flow above 1 bar after 200 days which is consistent with, for example, Showman et al. (2008). Even if we tend to find slightly faster equatorial jets, the zonally averaged structure described above compares favorably with results published in the literature that use a similar cooling function (Showman et al. 2008; Rauscher & Menou 2010; Heng et al. 2011b; Mayne et al. 2014a). One difference, though, is that we find weaker westward jets at high latitudes (with maximum westward winds of 100 m.s^{-1} compared to typical published values that are about one order of magnitude larger). This difference is most likely due to the fact that we are using a Cartesian coordinates system, as opposed to the spherical geometry that is commonly used. We have checked that the total (i.e. volume integrated) angular momen-

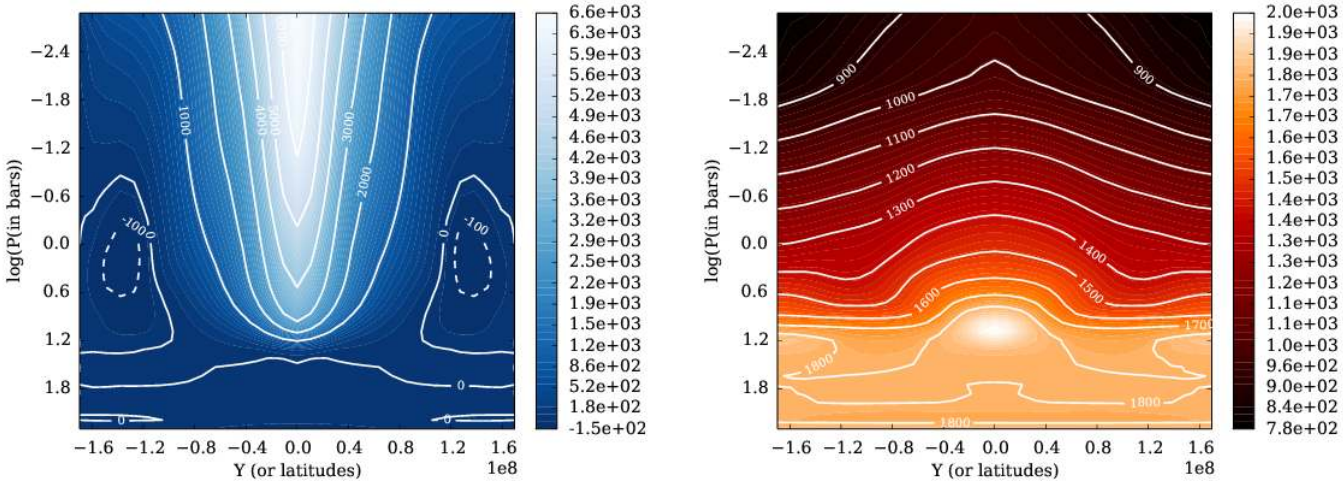

Fig. 1: Color contours of the time averaged zonal mean zonal velocity (*left panel*) and temperature (*right panel*) in the (y, P) plane for the low resolution model. The time average is performed from $t = 200$ days to $t = 500$ days using 300 snapshots.

tum is conserved in our calculations. In the equatorial β–plane approximation, the latter takes the form

$$M = \iiint \rho \left(u - \frac{1}{2}\beta y^2 \right) d\tau \,, \tag{11}$$

where the integral should be taken over the computational domain. We have found that M is conserved to within 2% in model 128x33 over the 500 days of integrations (with the small change being associated with a small leakage through the meridional boundaries of the domain). The weakness of westward jets in our simulation is something to keep in mind when comparing our results with previously published models.

The day/night heating contrast results in strong zonal asymmetries in both the dynamical fields and the temperature. These asymmetries are stronger in the atmosphere upper layers and gradually decrease downward. This is illustrated in figure 3, which shows the temperature and horizontal winds in the (x, y) plane at the pressure levels 1.66 mbars, 100 mbars and 4.4 bars. The first two panels zonal asymmetries are large because of the short radiative timescale at those locations. For example, at 1.66 mbar, the maximum (resp. minimum) velocity amounts to 7.1 km.s^{-1} (resp. 5.5 km.s^{-1}) and temperatures range from about 700 K to 1400 K. By contrast, the equatorial jet is essentially zonally symmetric at $P = 4.4$ bars, in agreement with previous results. At 100 mbars, we recover the chevron shape structure in the temperature reminiscent of previously published calculations. The structure of the flow at 1.66 mbars is interesting, as it illustrates one of the consequence of using the equatorial β plane model: while simulations performed on the sphere typically display a planetary scale Hadley cell, with upward motions in the substellar point and downward motions at the antistellar point, such a flow is impossible to obtain by definition in the framework of the equatorial β–plane model. Instead, meridional velocity are always deflected back to the equator since the Coriolis force becomes gradually stronger as y increases.

To conclude on section 3, the good agreement between the flow structure in our simulation, as shown on figures 1 and 3, with equivalent figures reported by Heng et al. (2011b), along with the fact that these results broadly agree with several studies of the same kind published in the literature, both validate our numerical implementation and the choice of our model parameters.

Model	N_x	N_y	U_{50}^{mean} m.s^{-1}	U'_{50} m.s^{-1}
LowRes	64	33	6158	-
128x33	128	33	6117	1.1
128x65	128	65	7390	18.6
128x109	128	109	7703	66.8
128x195	128	195	7957	124.3
256x65	256	65	7371	-
512x65	512	65	7226	-
1024x65	1024	65	7511	-
HighRes	1024	195	7731	207.3

Table 1: Model properties. Col. 1 gives the model label. Col. 2 and 3 features the horizontal resolution. Col. 4 and col. 5 respectively gives the zonally and time averaged zonal wind and zonal wind fluctuations at (see text for details on its calculation) 50 mbars. All the other parameters of the models are identical and described in section 2. Data are averaged between $t = 200$ and $t = 400$, except for the models having a $N_y = 195$ for which the averaging is performed between $t = 170$ and $t = 280$.

4. Resolution study

We next investigate the sensitivity of the properties described above to variations in the horizontal spatial resolution. All of the other parameters of the simulations are kept fixed. We vary N_x from 64 to 1024 and N_y from 33 to 195. The simulations parameters and their outcomes are summarized in Table 1. All runs but one are integrated for 400 days. Model HighRes, with a resolution of $(N_x, N_y) = (1024, 195)$, is computationally demanding. To reduce part of the burden, we restarted model 1024x65 at $t = 100$, multiplying the number of cells in the y direction by a factor of three. Integrations of the equations was then performed for another 350 days.

4.1. Effect on the climatology

All models qualitatively display the same climatology as described above. However, quantitative measures vary. As an example, we report on Table 1 (forth column, see also fig. 4) the

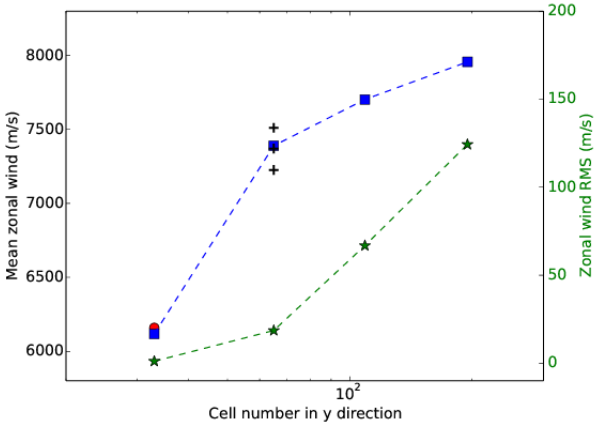

Fig. 4: Left axis: variations of the 50 mbars zonally and time averaged zonal mean wind at the equator with N_y. The blue squares corresponds to the models having a zonal resolution $N_x = 128$, the red circle shows model LowRes and the black pluses shows the results of the models having a meridional resolution $N_y = 65$ and varying number of cells in the zonal direction. Right axis (green stars): variations of the amplitude of the high frequency fluctuations of the zonally averaged zonal wind fluctuations (see text for details on its calculation) with N_y for the series of models having $N_x = 128$.

zonally and time averaged (between $t = 200$ and $t = 400$) zonal wind at the equator at the pressure level $P = 50$ mbars. We note that the equatorial jet is still being slightly accelerated over that period and has not yet reached a perfect equilibrium. For example, in model 128x65, the zonal wind at 50 mbars increases from 7.1 to 7.4 km.s^{-1} over that period (which represents less than 5%, a rather small acceleration that justify the claim made above that the flow is close to a steady state). Taken as a whole, this resolution study shows a strong sensitivity to the meridional resolution N_y (see the blue squares) but a very weak sensitivity to the zonal resolution N_x (see the symbols that correspond to $N_y = 65$ and varying N_x, all clustered at a mean zonal wind of about 7.2–7.3 km.s^{-1}). This difference comes from the different spatial scales of the equatorial jet in the x and y directions, namely a sharp meridional velocity gradient but a large scale longitudinal structure. In model LowRes, grid cells have a meridional extend of $dy = 10^7$ meters which means that the jet is only resolved with a handful of grid points (see the jet meridional size in figure 1) and is severely affected by numerical dissipation. Quite differently, the zonal variations of the jet have a typical scale comparable to the zonal computational domain itself (simply because thermal forcing is modulated on that scale) and is easily resolved with a few tens of cells in all of our models.

4.2. Shocks

As discussed in the introduction, it has been a long standing issue to determine whether or not shocks exist in hot Jupiter atmospheres. In our simulations, we have not found any signatures of shocks that would be traced by a sudden decrease of the local Mach number or a rapid increase of the density. As a more quantitative diagnostic, we have computed a dimensionless measure

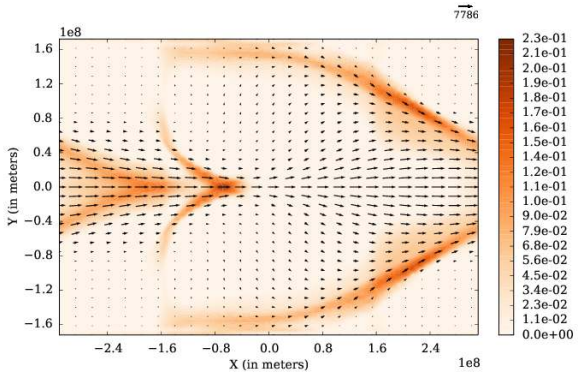

Fig. 5: Spatial distribution of η at the pressure level $P = 1.66$ mbars in model 128x65 (color contours). The arrows show the amplitude and direction of the hozizontal wind.

of the flow divergence, as done recently by Zhu et al. (2013):

$$\eta = \max\left(0, -\frac{dx}{c_s}\boldsymbol{\nabla}\cdot\boldsymbol{v}\right), \quad (12)$$

where dx denotes the cell size in the radial direction. In shock capturing scheme such as RAMSES, the numerical algorithm is designed to spread shocks over only a handful of cells, so we would expect η to reach at least a few tens of percent in shocks and be *independent of spatial resolution*. In fact, Zhu et al. (2013) argue that $\eta > 0.2$ is a good criterion for detecting strong shocks in their simulation. Since shocks are spread over a few cells in finite volume codes such as RAMSES, such a threshold indeed corresponds to a velocity jump larger than the sound speed across a discontinuity (or, using the Rankine-Hugoniot conditions, to an upstream Mach number larger than ~ 1.5).

In general, we have found that η only amounts to a few percents at pressure larger than a few tens of mbars, and decreases downward. For example, in model 128x65, its maximum value reaches 0.045, 0.034 and 0.022 at pressure levels $P = 50$ mbars, 100 mbars and 1 bars, respectively. η only takes significant values at pressure of a few mbars, as illustrated on figure 5. At such a low pressure, three zones feature values of η in excess of 10%. The first two are symmetric around the equator and located on the jet wings, for positive values of x. We note that they also manifest themselves by an increased temperature (see figure 3). It is likely that these two compressive regions are an artefact of the equatorial β–plane model that prevents an hemispheric Hadley cell from developing around the planet. The last zone with a large η is located at $x \sim -0.8$ around the equator and corresponds to the region where the zonal wind is strongly decelerated when entering the day side of the planet. η reaches 23% at that location in model 128x65. As emphasized by Heng (2012), this is the location where shocks would most easily form. However, here, it appears that this zone is only a region of large compression, but not a shock. Indeed, we found that η gradually decreases when the zonal resolution is increased, reaching 12% in model 256x65 and only 6% in model 512x65. This gradual decrease shows that the zonal wind decline when entering the planet day side is smooth and converged upon increasing the resolution, as opposed to a shock that would steepen and be caracterized by a constant, large η value. We note that the two symetric high η regions on figure 5 show the same trend with resolution, which means that these two zones are also regions of

adiabatic compression. We conclude from this analysis that the mean flow in the atmosphere of hot Jupiters displays no shocks.

4.3. Time variability

We also computed an estimate of the high frequency rms fluctuations U'_{50} of the zonally averaged equatorial zonal wind at 50 mbars (see last column on table 1 and green symbols on figure 4 for the models with $N_x = 128$). To do so, we first subtracted the low frequency component of the wind by smoothing the raw data with a Hamming function having a 20 days width. U'_{50} is then simply the root mean square of that signal. While it is very small when $N_y = 33$, we find that U'_{50} increases steadily and amounts to more than 100 m.s^{-1} for model 128x195 and about twice that value for our highest resolution model HighRes (not shown on figure 4). We now focus on this last model in order to investigate the physical origin of that variability.

5. High resolution model

The nature of the zonally averaged zonal wind variability in model HighRes is best illustrated by showing the time variation of the vertical profile of the zonal wind at the equator $\overline{U_{eq}}$ (figure 6, top panel). The difference with figure 2 is striking: $\overline{U_{eq}}$ shows significant variations during the entire duration of the simulation. These variations takes the form of quasi–periodic oscillations of the zonal wind, with a period of about 10 days, during the first half of the simulation ($t < 300$) and are less regular, but still significant, at later times. The zonal wind variations are in phase from the top of the planet atmosphere down to the inert layer below 10 bars, which is most likely a result of the fast communication timescale across the atmosphere provided by sound waves. The time history of $\overline{U_{eq}}$ at $P = 50$ mbars is shown on figure 6 (bottom panel). In fact, we can distinguish three phases of the zonal wind evolution (indicated with labels on the upper part of both panels): "Phase I" ($t = 100$ to $t = 170$) is a spin–up phase during which the flow adjusts to the sudden change in meridional resolution. In agreement with the results of section 4, the zonal wind rapidly increases by about 1 km.s^{-1} over a period of just a few days. We call "Phase II" the period that extends between $t = 170$ and $t = 270$. The flow appears to have reach a "quasi–steady state" over that period (see also the top panel of the same figure that suggests that this is the case at all levels above a few bars) and the zonal wind displays quasi–periodic oscillations around a well–defined mean value. At 50 mbars, the zonally averaged zonal wind fluctuations are significant and amount to almost 1 km.s^{-1} between its largest and smallest values. We investigate in detail the flow properties during "Phase II" in section 5.1. At time $t \sim 270$, this quasi–periodic evolution of the wind seems to come to an end and the mean zonal wind decreases. This is what we call "Phase III" of the flow evolution. As shown by the solid contours on figure 6 (top panel), the beginning of that phase coincides with a significant decrease of the Richardson number Ri. The latter is defined by the relation

$$Ri = \frac{N^2}{(\partial U/\partial z)^2}\,, \tag{13}$$

where N^2 stands for the Brunt–Vaisala frequency and is calculated according to

$$N^2 = \frac{\rho g^2}{P}\left[\left(\frac{d\ln T}{d\ln P}\right)_S - \left(\frac{d\ln T}{d\ln P}\right)\right], \tag{14}$$

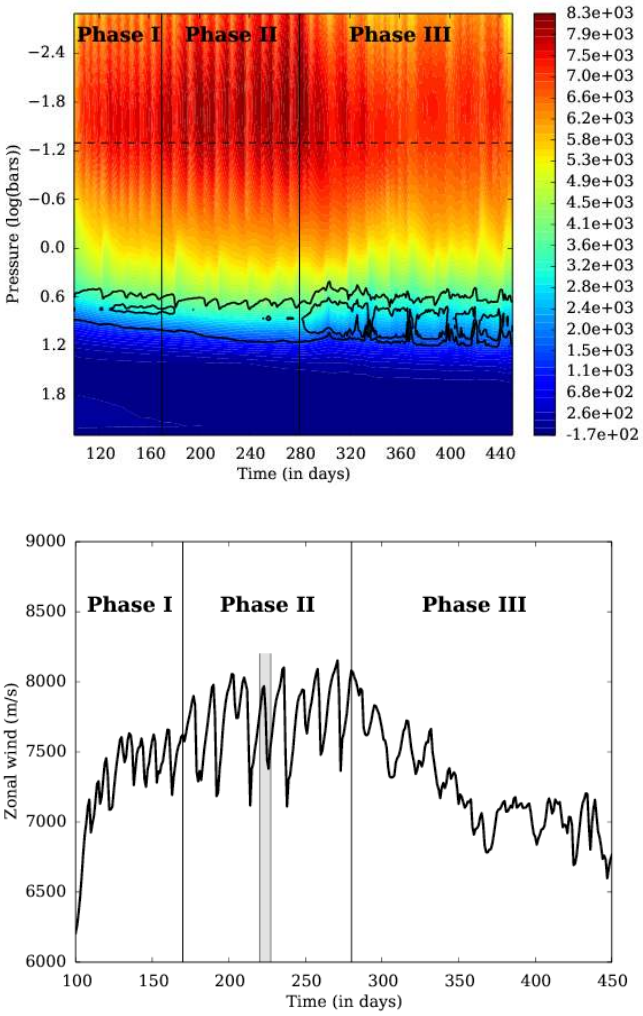

Fig. 6: Top: evolution of the vertical profile of the zonally averaged zonal wind at the equator in a time-pressure plane for model HighRes. The horizontal dashed line marks the 50 mbars level. The solid lines are contours of the zonally averaged Richardson number (see text). The contours are for 0.1 (interior contour) and 0.25 (exterior contour). Bottom: time variations of the zonally averaged zonal wind at the equator at the pressure level $P = 50$ mbars for model HighRes (see text for a discussion of the three phases displayed on both panels).

is which the first term inside the square bracket denotes the isentropic gradient. As discussed by Showman & Guillot (2002) in the context of hot Jupiter atmospheres and later investigated in more details by Li & Goodman (2010), sheared flow in stratified atmospheres are prone to a vertical shear instability when Ri is smaller than a threshold value that depends on the gas thermodynamics but is of order 1/4. In our simulation, the coincidence between the end of Phase II and the appearance of zonally averaged Richardson numbers smaller than 0.1 suggests that such an instability develops at that time and starts perturbing the flow. In section 5.2, we will investigate "Phase III" in more details and give compelling evidences that this is indeed the case.

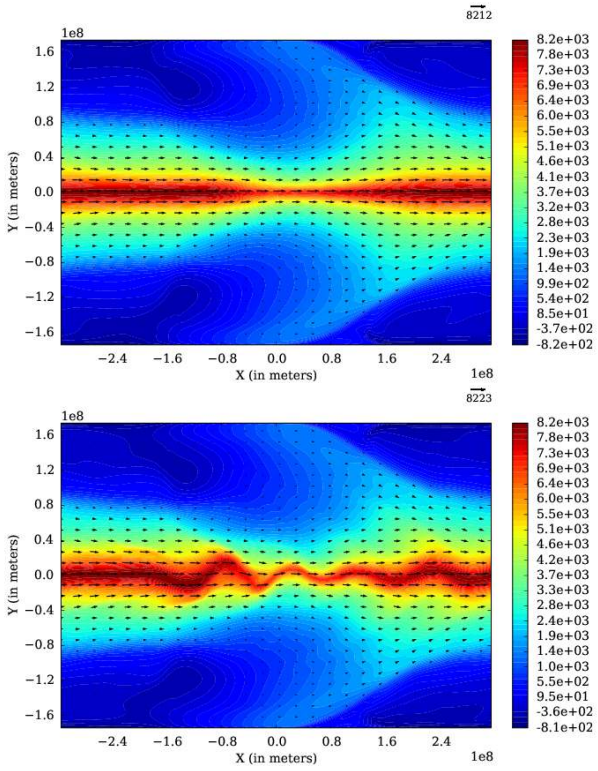

Fig. 7: Color contours showing the horizontal distribution of the zonal wind at time $t = 208$ (*top panel*) and $t = 213$ (*bottom panel*) in model HighRes at $P = 10$ mbars. The arrows display the horizontal wind vectors. Note the clear meanders of the equatorial jet in the bottom panel as opposed to the more zonal structure of the equatorial jet in the top panel.

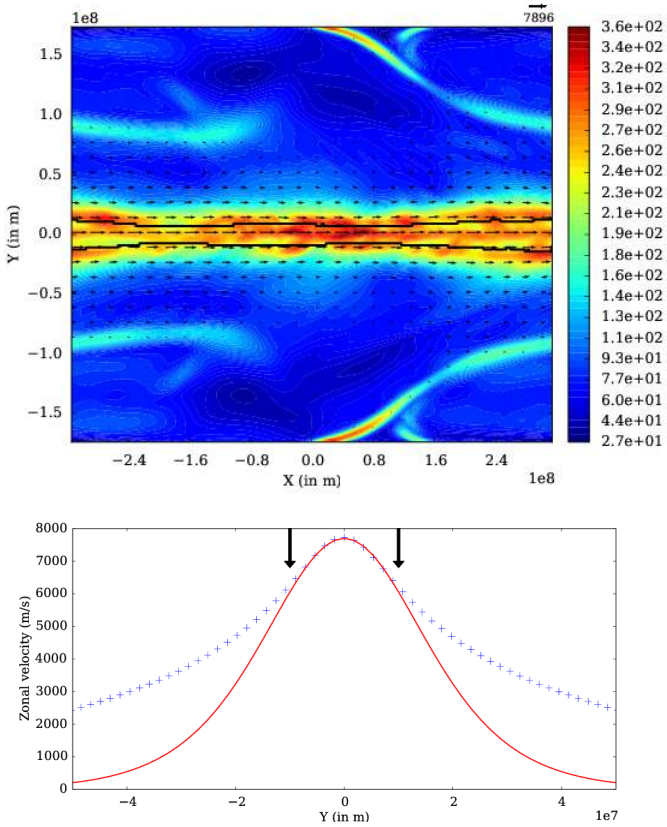

Fig. 8: Top: color contours show the rms of the eddy specific kinetic energy ($u'^2 + v'^2$) spatial distribution in the horizontal plane at pressure level $P = 50$ mbars for model HighRes (during phase II of the evolution) while arrows display the steady component of the wind over the same time interval. The thick solid line plots the locus of the points where the meridional gradient of total vorticity (planet+flow) vanishes. Bottom: y–profile of the time-averaged zonal velocity (during Phase II) at the vicinity of the equator and at pressure level $P = 50$ mbars for model HighRes (blue crosses) compared with a Bickney jet profile (red line – see text for details). The two vertical arrows mark the location of vanishing meridional gradient of total vorticity.

5.1. A barotropic Kelvin-Helmholtz instability (phase II)

5.1.1. Equatorial jet variability

During "phase II" of model HighRes, the equatorial jet periodically alternates between two states, during which it is either almost perfectly zonal in the vicinity of the equator or display meanders (figure 7). The jet velocity increases when the jet is zonal and slows down when the meanders amplitude saturates and decreases. To make further progress, we next decomposed the horizontal velocity as the sum of a time averaged component and a fluctuating part:

$$\boldsymbol{v}(x, y, t) = \overline{\boldsymbol{v}}(x, y) + \boldsymbol{v}'(x, y, t)\,, \tag{15}$$

where the time averaged is performed using 100 dumps evenly spaced between $t = 170$ and $t = 270$. In the following, we will use the notations $\overline{u}$ (resp. $\overline{v}$) and u' (resp. v') to denote the x (resp. y) component of these velocities. Using this decomposition, we define the specific kinetic energy of the fluctuations as

$$E_K = u'^2 + v'^2\,, \tag{16}$$

and the meridional gradient of the total vorticity of the flow (including the planetary scale vorticity associated with Ω_p):

$$\xi_y = \frac{\partial \xi}{\partial y} = \beta - \frac{\partial^2 \overline{u}}{\partial y^2}\,. \tag{17}$$

Taking advantage of the barotropic nature of the flow (figure 6, top panel), we now focus on its structure at the 50 mbars pressure level until the end of this section.

Figure 8 (top panel) shows that the time averaged value of the rms of E_K over "Phase II" reaches values of the order of a few hundred m.s^{-1} at 50 mbars in the jet core, interior to the region where ξ_y vanishes, and drops rapidly as one moves outward of that region. It is a well–known result of hydrodynamics that the presence of two extrema in the flow vorticity profile (such as shown on figure 8) is a necessary condition to destabilize a two–dimensional incompressible flow (see for example Vallis 2006). Here, the flow is compressible, stratified and three dimensional, and such a simple criterion does not apply, strictly speaking. Nevertheless, we can still expect that it remains a good guide for linear stability because the deviations from both compressibility and two–dimensionality are small. The rapid drop of E_K outside of the two locations where ξ_y vanishes also argues in favor of this interpretation and strongly suggest that the jet is subject to a Kelvin-Helmholtz instability that originates from the velocity meridional gradient and drives the oscillations seen during Phase II.

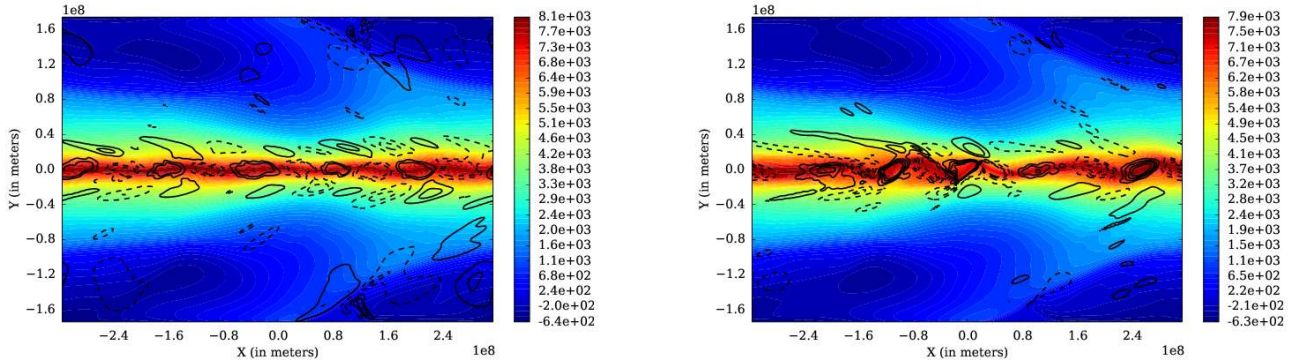

Fig. 10: Color contours showing the horizontal spatial distribution of the zonal wind at $P = 50$ mbars at times indicated with red dots on figure 9, namely $t = 223.3$ (*left panel*) and $t = 224.7$ (*right panel*). Black contours plots the meridional velocity fluctuations v'. Contours are shown every 50 m.s^{-1} from -100 to 100 m.s^{-1} on the left hand side panel and every 100 m.s^{-1} from -400 to 400 m.s^{-1} on the right hand side panel. On both panels, positive (resp. negative) contours are shown with solid (resp. dashed) lines and the zero contour is omitted.

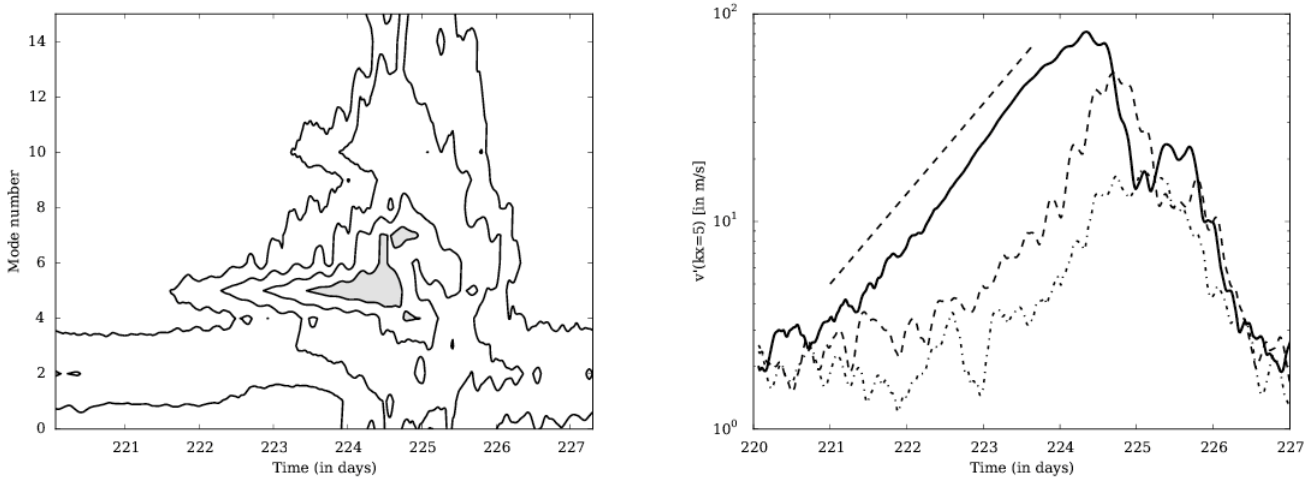

Fig. 11: Left: Amplitude of the meridional velocity fluctuations Fourier transform $\tilde{v}'(k_x, t)$ in the (k_x-time) plane for model HighRes, spatially averaged over the region $|y| < 5 \times 10^7$ meters. Contours are for $log(\tilde{v}'_{max}/2)$, $log(\tilde{v}'_{max}/4)$, $log(\tilde{v}'_{max}/8)$ and $log(\tilde{v}'_{max}/16)$. The region surrounding the maximum is filled in gray. Right: Same as the left panel, but showing the time evolution of particular modes, namely: $k_x = 5$ (*thick solid line*), $k_x = 7$ (*dashed line*) and $k_x = 9$ (*dotted–dashed line*). The straight dashed line represents an exponential growth with a timescale of 1 day.

5.1.2. Linear instability properties

To investigate that possibility in more details, we next focus on a single oscillation of the jet. It is highlighted as the region shaded in light gray in figure 6 (bottom panel). In practice, the analysis that follows was conducted by restarting model HighRes at $t = 220$ for about 7 days, saving the simulation data every 4000 seconds in order to sample the fluid evolution at high frequency. Figure 9 shows that the rms fluctuations of v' at the equator (solid blue curve), initially of the order of 20 m.s^{-1}, grows during about 3 days until they reach an amplitude of ~ 350 m.s^{-1} after which they decay in roughly one day. The spatial structure of these fluctuations is further illustrated on figure 10 using two snapshots that illustrate the growing (left panel) and maximum (right panel) phases of the evolution. During the growing part (here plotted at $t = 223.3$), v' clearly displays a regular and oscillating pattern at the equator, with a well–defined spatial period of 1/5th of the domain size, suggestive of a linear modal growth. The background jet structure is only weakly modified during that phase. Note that the jet velocity reaches its maximum at that point (black curve on figure 9). By time $t = 224.7$, the velocity fluctuations have grown significantly and show clear signs of saturation, as evidenced by positive and negative contours colliding with each other. Before looking at this saturation phase in more details in the next paragraph, we first quantify the properties of the fastest growing mode of the instability by performing a spectral analysis of the flow properties. This was done by computing the amplitude of the Fourier coefficients of $v'(x, y, t)$ in the zonal direction. We then spatially averaged those coefficients in the vicinity of the planet equator and show their variations as a function of the normalized zonal wavenumber k_x and time on

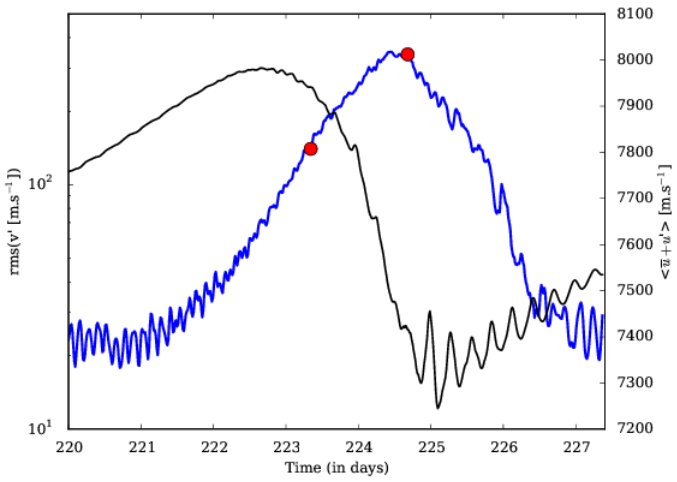

Fig. 9: Time evolution of the root mean square of the meridional velocity fluctuations v' (blue curve – see text for details) and mean jet velocity (black curve) at the equator. The red circles indicate the different time at which the jet structure is plotted on figure 10.

figure 11 (left panel)[2]. From $t = 222$ to $t = 224$, the flow evolution is dominated by the $k_x = 5$ mode. Consistent with the idea of a linear instability, that mode grows exponentially with a typical timescale of about 1 day (fig. 11, right panel). It reaches its maximum amplitude at $t \sim 224$, shortly after higher k_x modes amplitudes also start to grow, presumably as a result of nonlinear interactions with the $k_x = 5$ mode. This later growth of higher k_x modes is illustrated on the right panel of figure 11 for the particular cases of the modes $k_x = 7$ and $k_x = 9$. At $t = 225$, a large range of spatial scales , with wavenumber k_x up to 15 (see left panel of figure 11), have reached a significant amplitude. During the entire duration of this additional simulation, we also find that larger scale modes (with k_x ranging from 1 to 3) have significant amplitudes. Their evolution, however, is quite different from the modes with $k_x \geq 5$. They do not display any signature of an exponential growth and their amplitude is modulated by no more than a factor of two during the simulation. It is likely that these properties reflect the nonlinear feedback of the instability on the large scale structure of the equatorial jet.

To summarize, we have determined the wavenumber of the most unstable mode of the instability ($k_x = 5$) and its growth rate ($\sigma = 1$ day^{-1} $= 3.5 \times 10^{-6}$ s^{-1}). In principle, these properties (as well as the mode phase velocity, see below) could be compared to the result of a numerical linear instability analysis. However, for a 3D compressible flow, such an analysis is tedious and beyond the scope of this paper. Here, we only provide a very crude estimate of these properties based on 2D incompressible flows. A useful and well studied example of such flows is the so–called Bickney jet, for which the jet profile is given by

$$U(y) = U_B \, \mathrm{sech}^2\left(\frac{y}{L_B}\right), \qquad (18)$$

where the parameters U_B and L_B caraterize the jet. The Bickney jet is known to be unstable to the Kelvin-Helmoltz instability and the most unstable wavelength satisfies the relation $k_x L_{jet} \sim 1$ (Drazin & Reid 1981). The core of the jet in our simulations (i.e. within the region where the vorticity is maximum) can be well fitted by the Bickney jet meridional profile (see figure 8, bottom panel) for which $L_{jet} = 2\times10^7$ meters. Given the size of our computational box and the above scaling, this is consistent with the instability having a most unstable wavenumber $k_x = 5$, as seen in the simulations. However, in this case, the predicted growth rate σ_{th} is of the order of $\epsilon k_x U_B$, with $\epsilon \sim 0.15$. This translates into a growth rate that is more than an order of magnitude larger than measured in the simulation. This large disagreement illustrates the limit of a naive 2D reasoning and suggests that three–dimensional effects, compressibility, or the finite resolution of our simulations likely affect the flow. More work is needed to clarify the properties of the instability, and, more importantly, the conditions under which it develops.

5.1.3. Nonlinear saturation (due to shocks?)

As mentioned above, the background jet becomes significantly distorted when the amplitude of the perturbations reaches large amplitudes (see right panel of figure 10). The nonlinear interaction that results quickly damps the flow velocity fluctuations, the jet slows down (black curve on figure 9) and return to a more zonal structure such as shown on figure 7 (top panel). We have found temperature fluctuations of a few hundred Kelvin during that phase (figure 12, bottom panel). They tend to be associated with the region of the jet that displays the largest meanders (figure 12, top panel). In addition, sharp features in the zonal velocity (such as seen at the location $x \sim -0.2\times10^8$ and $y \sim -0.1\times10^8$ for example) are ubiquitous in snapshots of the flow during the nonlinear stage of the instability.

For these reasons, and because of the supersonic nature of the jet velocity, it is natural to ask whether saturation occurs via shocks. Detecting shocks in 3D non–steady flows is known to be extremely difficult to achieve in a systematic manner. Here, we only give a couple of simple arguments that suggest that shocks play no role in the instability saturation. First, as in section 4.2, we computed the distribution of η given by Eq. (12). We again found that the maximum value of η never exceeds a few percents at 50 mbars (and, in fact, at all pressure levels). The sharp gradients mentioned above in the zonal velocity are in fact compensated by regions with significant vertical downward flow. This suggests that the nonlinear saturation of the instability is not associated with large compressive events.

A second argument is that, in the frame where the shock would be stationary, the flow is actually just about sonic. This can be seen by plotting the equatorial meridional velocity fluctuations in a spacetime diagram in the (x, t) plane, also known as an Hovmöller plot (see figure 13). It shows that the eastward velocity of the growing wave pattern amounts to about 6 km.s^{-1} (see solid black line)[3]. Because the flow velocity in the frame rotating with the planet reaches at most 8 km.s^{-1} (see upper panel of figure 12), this means that the zonal wind velocity upstream of a putative shock would be smaller than 2 km.s^{-1} in the frame in which the flow structures are stationary. This is comparable to (and in fact, slightly smaller than) the sound speed, so that the flow Mach number is at best of order unity. If shocks exist, they are only weak shocks, with upstream Mach number of order 1 at best. More work is needed to characterize the dynamical mechanism responsible for the saturation and to investigate

[2] The zonal wavenumber is defined such that $k_x = 1$ corresponds to a wavelength equal to the size of the domain in the x–direction.

[3] This velocity also corresponds to the phase velocity of the linear instability discussed above

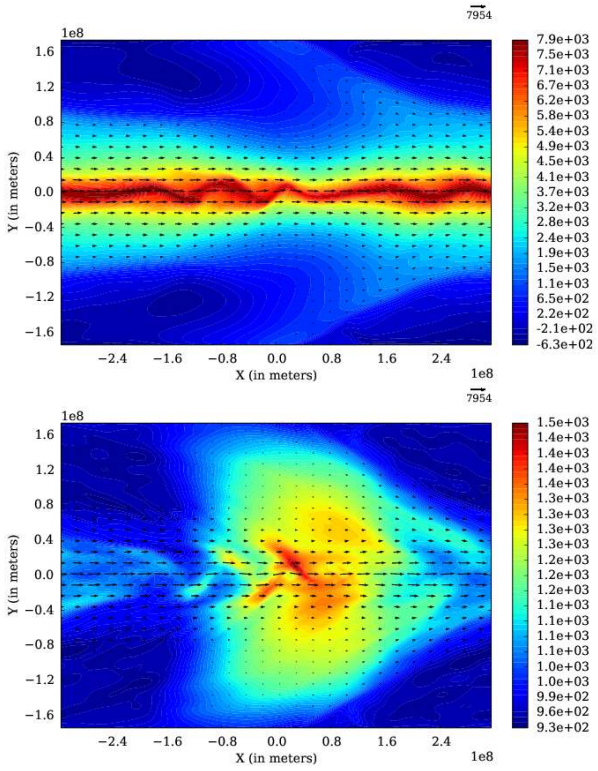

Fig. 12: Zonal velocity (*top panel*) and temperature (*bottom panel*) at time $t = 224.7$ in model HighRes (i.e. when velocity fluctuations reach their maximum value) at pressure level $P = 50$ mbars. Jet meanders upstream of the substellar point, located at $(x, y) = (0, 0)$, are clearly associated with temperature fluctuations.

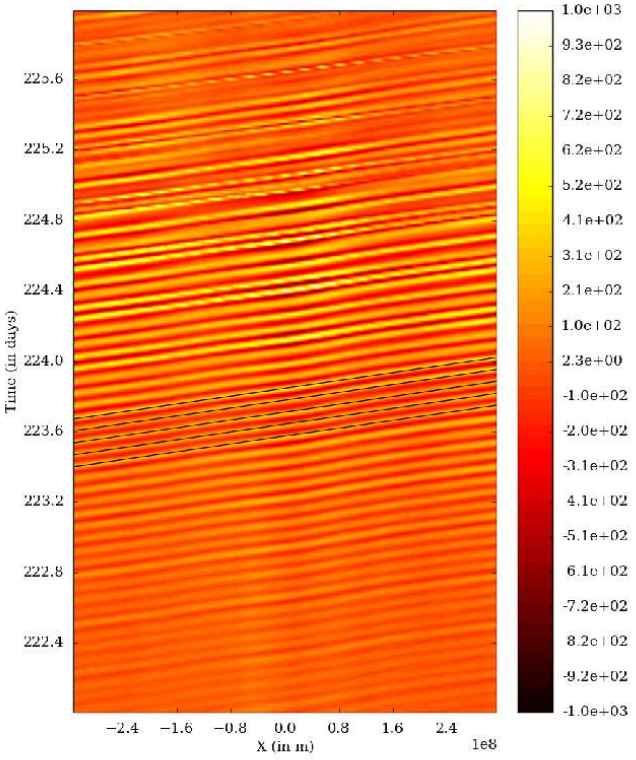

Fig. 13: Hovmöller space–time diagram of the meridional velocity fluctuations v' at the equator in model HighRes at pressure level $P = 50$ mbars. The thin black lines have a 6 km.s^{-1} slope.

whether that result holds across the entire parameter space, but the present simulation seems to rule out the presence of shocks, at least for the set of parameters we considered.

5.2. A vertical shear instability (phase III)

The nature of the flow changes during phase III of the simulation. A typical snapshot of the equatorial zonal wind in the (x, P) plane during that phase is plotted on figure 14 (left panel, here shown at $t = 319$). It demonstrates that the zonal wind at the equator displays high frequency variations in the x–direction that seem to extend over the entire atmosphere.

5.2.1. Identification of the instability

By-eye measurement of the oscillations spatial period (figure 14, right panel, see the black horizontal line) gives a typical value of about 8000–10000 km. By comparison, the most unstable mode of the vertical shear instability has a typical wavenumber k_x that satisfies the relation $k_x H \sim 0.5$ (Li & Goodman 2010). For temperature of about 1800 K such as we use here, the associated wavelength amounts to about 11000 km, remarkably close to our measurement. As an additional diagnostic, we plot in figure 15 a spacetime diagram of the high frequency component of the zonal wind (hereafter noted δu). The latter is calculated by applying a high–pass filter to individual snapshots such as shown on figure 14. To do so, we use a Hamming function with a half width of 30 zonal cells as a low pass filter, and subtract the low–pass filtered data to the raw data. The comparison with the Richardson number (solid contours on figure 15) shows a clear positive correlation: at the bottom of the atmosphere ($P \sim 1$–10 bars), δu displays a local maximum at pressure depth for which Ri drops below $1/4$. In addition, that maximum is larger when Ri is smaller (see the difference between phase II and phase III of the simulation, or the increase of δu at $t \sim 150$ that is coincident with a period of smaller Ri values). Taken together, these results are consistent with the analysis of Li & Goodman (2010) and strongly suggest that the vertical shear instability operates at pressure levels where the Richardson number reaches zonally averaged values smaller than $1/4$.

5.2.2. Formation of shocks in the upper atmosphere

Figure 15 also shows that δu increases strongly in the atmosphere upper layers, reaching values of up to a few hundred m.s^{-1} at pressure levels of a few mbars. It is also clear that these velocity fluctuations are connected to the atmospheric activity at 10 bars. Future work is needed to investigate their exact origin, but it is plausible, as recently suggested by Cho et al. (2015) in another context, that they are gravity waves triggered by the vertical shear instability that propagate upward and amplify as the density decreases.

Because these fluctuations reach large amplitudes in the upper atmosphere, we have closely investigated whether or not they eventually steepen into shocks. In agreement with the findings of

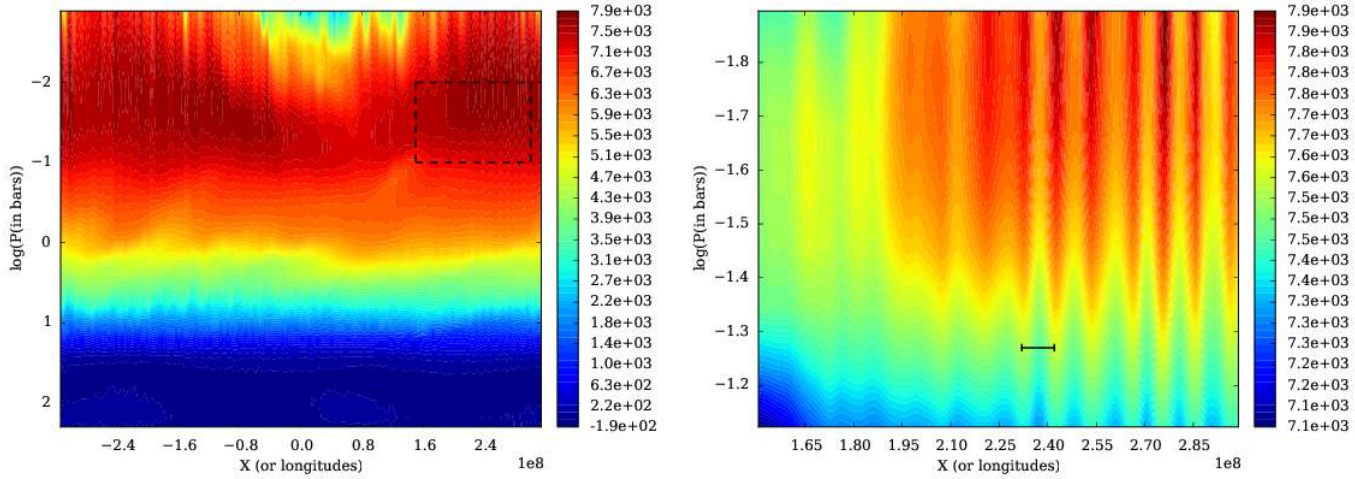

Fig. 14: Zonal velocity at the equator in a (x, P) plane at time $t = 319$ in model HighRes (*left panel*). Note the high frequency variations of the velocity (particularly easy to see in the atmosphere upper layers), superposed on the large scale zonal and vertical variation of the equatorial jet velocity. The right panel shows an enlargement of the dashed box shown on the left panel. The horizontal bar has a length of 10000 km.

the preceding sections, the flow remains devoid of such shocks at pressures larger than $\sim$ 10 mbars, with η being of the order of a few percent at most. However, we have found signatures of weak shocks in the top layers of the atmosphere. As an example, we show on figure 16 that the zonal wind at $P = 1.66$ mbars displays large and high frequency variations near the equator, accross which the zonal velocity appears to decrease by a few km.s^{-1}. These fluctuations are associated with values of η up to 35% and also display significant increase of the temperature by a few hundreds Kelvin (see figure 17, left panel). Given the short radiative timescale at this pressure ($\sim 10^4$ seconds), such significant temperature fluctuations are indications of fast dynamics. We thus focused on one of these structure (marked as a dashed line of the left panels of figure 17), and plotted the profiles of the zonal wind and of the temperature along that line (figure 17, right panel). There is a clear discontinuity in both profiles at $x \sim 1.72 \times 10^8$m that we identify as a shock. At that location, the zonal velocity rapidly decreases from 7 km.s^{-1} to 4 km.s^{-1} within a handful of cells. Simultaneously, the temperature increases from $\sim$ 800 K to about 1050 K. We measured the shock front velocity V_{sh} by restarting the simulation for a short amount of time, saving output data at a high frequency. We found for V_{sh} a value of the order of 3.9 km.s^{-1} (not shown), which, along with a typical sound speed of 2 km.s^{-1} at this location, indicate that the shock upstream Mach number is roughly $M_1 \sim 1.5$. The associated temperature discontinuity shown on figure 17 (right panel) can then be compared with the prediction of the Rankine-Hugoniot condition:

$$\frac{T_2}{T_1} = \frac{[(\gamma-1)M_1^2+2][2\gamma M_1^2-(\gamma-1)]}{(\gamma+1)^2 M_1^2}, \qquad (19)$$

where T_1 and T_2 are the upstream and downstream gas temperatures, respectively. For the case considered here ($M_1 = 1.5$ and $\gamma = 1.4$), Eq. (19) gives $T_2/T_1 = 1.32$, in very good agreement with the simulation (for which the ratio is about 1.35). This confirms that the numerous structures identified in figure 17 (left panel) with the contours of η are indeed shocks. We have not attempted to quantify the frequency, Mach number distribution

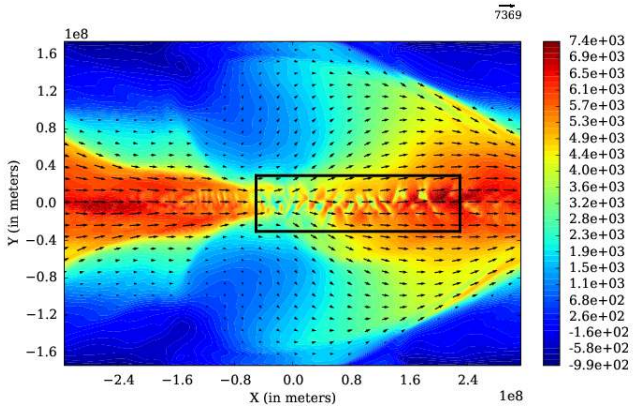

Fig. 16: Zonal velocity in model HighRes at $t = 335$ at the pressure level $P = 1.66$ mbars. Arrows indicate velocity vectors and the square marks the region studied in figure 17.

and preferred locations of these shocks. Besides being a difficult task on its own to be carried in a systematic manner, there are also limitations and artifacts of the present setup (see below) that have led us to postpone a detailed characterization of these shocks to future work.

5.2.3. Dissipation in the deep atmosphere and implications for the interior

Figure 15 also shows a significant increase of the temperature at $P \sim 10$ bars (see the white dashed contours) up to a temperature of about 2400 K (which should be compared to $T_{eq} = 1800$ K at that level). Again, there is a strong correlation between that rise and the flow activity, which suggests that the former is a consequence of the latter. This is not surprising and only a result of small scale kinetic energy being dissipated and transformed into heat. In RAMSES, such a thermalization is naturally captured because we solve the total energy equation and does not

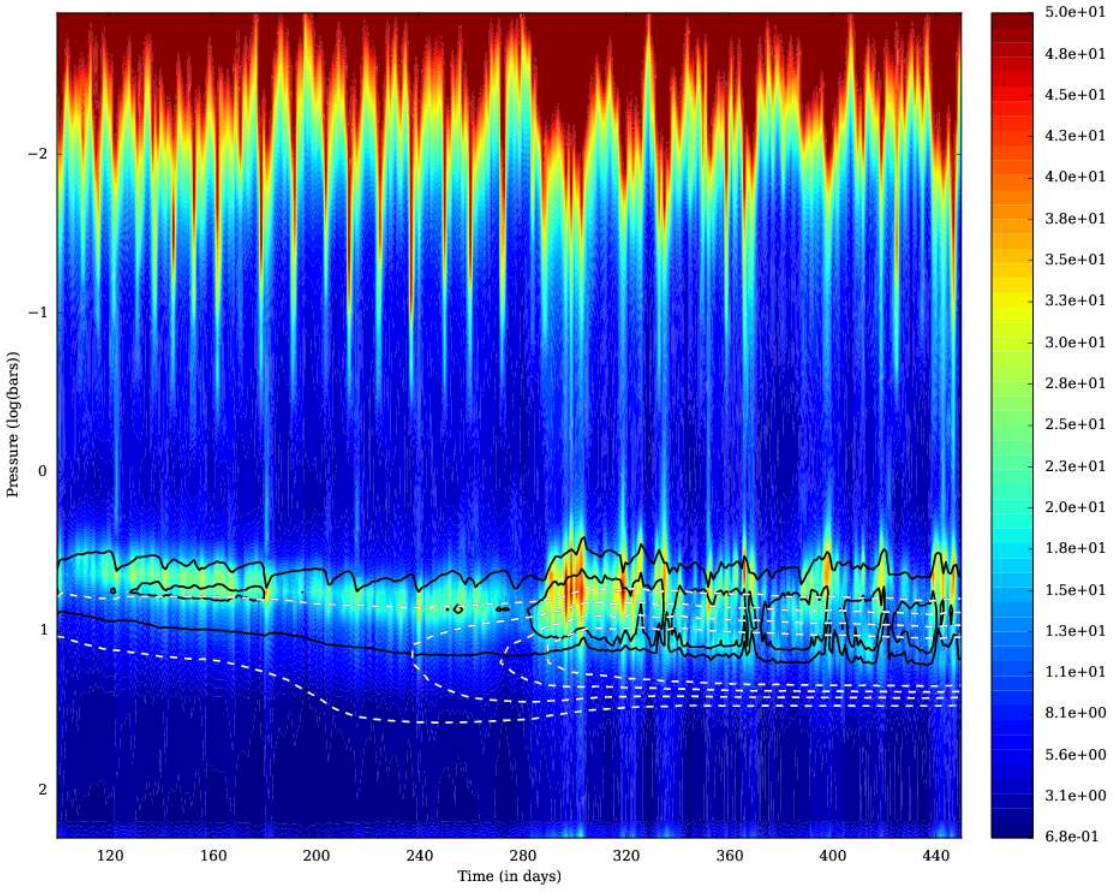

Fig. 15: Spacetime (time-pressure) diagram of the zonally averaged high frequency component of the zonal wind (see text for details) in color contours (note that the color table has been saturated at 50 m.s^{-1}). Contours of Ri (solid lines) and T (dashed lines) are overplotted. For Ri, contours are for $Ri = 0.1$ and 0.25. For the temperature, contours are for $T = 1900$, 2000, 2100 and 2200 K.

require using explicit dissipation coefficient (in that sense, the dissipation is solely numerical in origin). At 10 bars and below, the radiative timescale τ_{rad} goes to infinity and heated gas cannot cool radiatively anymore : in other words, heat deposited in the inert layer as a result of kinetic energy dissipation accumulates and temperature rises. As shown on figure 15, such an increase of the temperature at 10 bars also increases the vertical temperature gradient (in absolute value) and helps decrease the Richardson number through its dependence on the Brunt-Vaisala frequency. This effect can be quantified by measuring the kinetic energy flux in the vertical direction. To do so, we computed the kinetic energy flux per unit area according to the relation:

$$F_{KE}(P) = \frac{1}{L_x L_y} \iint \frac{1}{2} \rho v^2 v_z dx dy \,, \tag{20}$$

where the integral is calculated at the pressure level P. In both models LowRes and HighRes, figure 18 shows that we recover a negative vertical flux of kinetic energy, in quantitative agreement with Showman & Guillot (2002) and with a similar value of about -2000 to -3000 W/m^2. Note that this agreement is somewhat fortuitous and should not be taken too seriously: in the equatorial β–plane model such as used here, motions gradually go to zero away from the equator, so that F_{KE} depends on the arbitrary location of the boundaries in the y–direction. However, this qualitative agreement with Showman & Guillot (2002) supports the fact that the existence of this flux is robust.

Figure 18 also shows that a larger negative flux is present in the deep atmosphere ($P \sim$ 5–10 bars) in model HighRes than in model LowRes, precisely at the location where we see the temperature increase during Phase III. This additional flux is likely associated with the vertical shear instability and illustrates the idea of Showman & Guillot (2002) that downward kinetic energy transport can be associated with extra heating in the deep layers of the atmosphere. In addition to the increased kinetic energy flux suggested by figure 18, turbulence in stably stratified atmosphere also transports heat downward (Youdin & Mitchell 2010) and is likely at play here as well.

As first recognized by Guillot & Showman (2002), such downward energy fluxes are comparable to, and even greater than, the internal cooling flux of a typical inflated hot Jupiter. This mechanism—conversion of stellar energy into kinetic energy to be transported and dissipated deep in the atmosphere—is thus still a viable explanation to the problem of the large radius of highly irradiated giant planets. The main difficulty—a

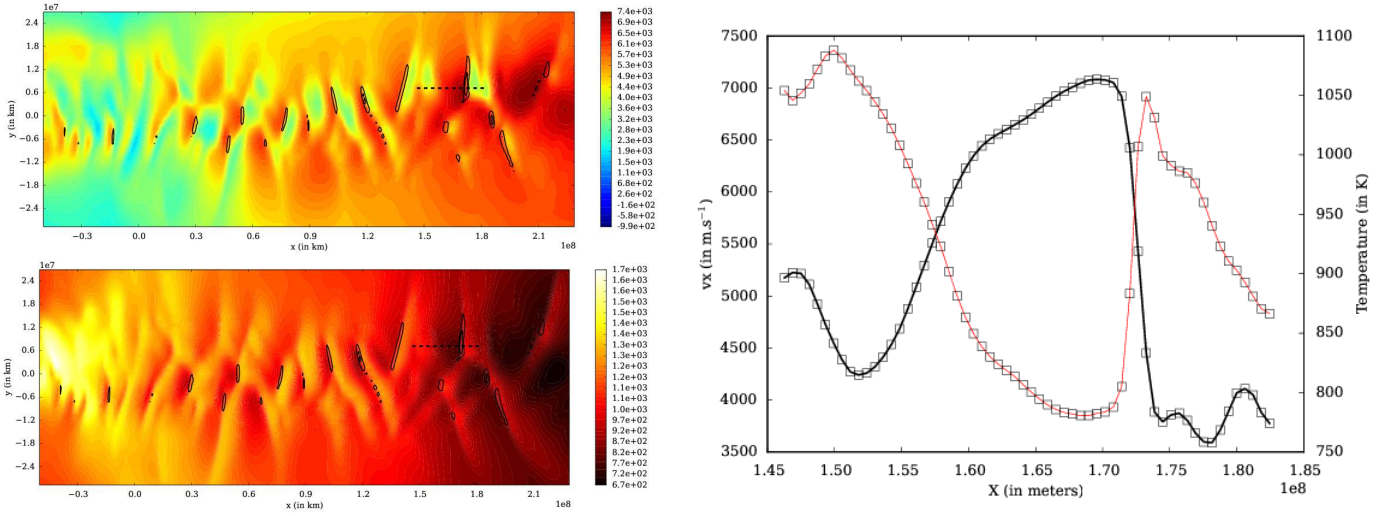

Fig. 17: Left: Color contours of the zonal wind (*top panel*) and temperature (*bottom panel*) at time $t = 335$ in the rectangle box depicted in figure 16. The contours shows the distribution of η, as given by Eq. (12). Levels are for $\eta = 0.1$ and 0.2. Right: Profiles of the zonal velocity (*black curve*) and temperature (*red curve*) along the dashed line shown on the left panels. For both curves, the empty squares marks the locations of the cells centers.

difficulty faced by most proposed mechanisms—is that this energy must be deposited deep enough inside the planet to significantly affect its thermal evolution (Ginzburg & Sari 2015), possibly in the deep adiabat (Guillot & Showman 2002). Depending on the precise planet and its age, Guillot & Showman (2002) predict this level to be in the 100–1000 bar range. Although figure 18 seems to imply that not much energy is deposited below the 10–20 bar level, it should be clear that, in our model, this *barrier* is most probably an artifact of the numerical setup. As discussed above, the presence of an inert layer below 10 bars, where τ_{rad} becomes infinite, provides a strong positive feedback on the wave activity and the heating at this level. If we had a more realistic, gentler increase of the radiative timescale, the level of maximum energy deposition would probably be pushed deeper. Indeed, we remark that figure 15 displays clear evidence of significant small scale activity at pressure levels of a few bars, i.e. largely above the inert layers, early in the simulation ($t < 300$ days). This is suggestive evidence that an infinite radiative timescale is *not* needed to trigger the vertical shear instability. But we cannot yet assess the maximum depth at which energy deposition will occur.

Therefore, while our model illustrates the possibility that vertical shear instability can develop in hot Jupiter atmospheres, their long–term effect on the flow remains to be determined with a more realistic treatment of the radiative properties of the deep atmosphere. Only then will we be able to properly quantify whether the mechanism first proposed by Guillot & Showman (2002) can realistically account for the inflated radius of strongly irradiated giant planets.

Before ending this section, and with the above caveats in mind, we stress that the effect of the vertical shear instability on the equatorial jet velocity is significant. While its time averaged value over phase II of the flow evolution is about 7700 m.s^{-1} at 50 mbars, the equatorial wind goes down to 6700 m.s^{-1} when averaged between $t = 400$ and $t = 450$. We have check that the spatial distribution of the temperature above 1 bar is almost identical during the two phases (not shown) and can not be incriminated for the jet velocity decrease. Rather, it is likely that

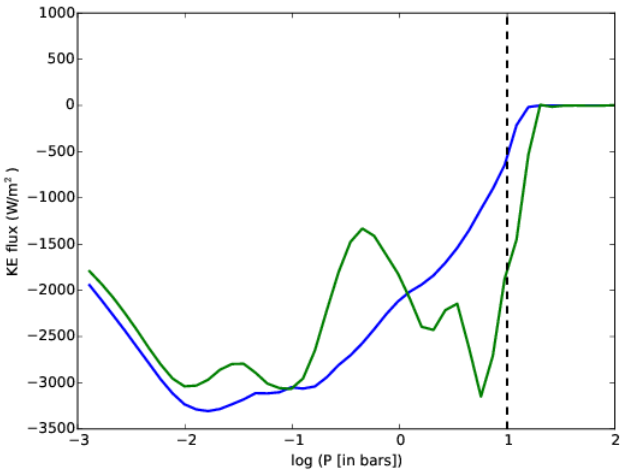

Fig. 18: Vertical profile of the kinetic energy flux during Phase III of model HighRes (*green curve*) and in model LowRes (*blue curve*), calculated according to Eq. (20). The dashed line marks the location of the top of the inert layer at 10 bars. Both curves are time averaged between $t = 350$ and $t = 450$.

the small scale velocity fluctuations associated with the vertical shear instability act as a form of drag that slows down the jet, possibly mediated by gravity waves (see Watkins & Cho 2010) and, as shown above, by shocks, both excited by the vertical shear instability. Given the limitations of the numerical setup used here, a detailed and quantitative investigation of that possibility is beyond the scope of this paper but opens up the possibility for developing a physically motivated subgrid scale model for the dissipation in the atmosphere of hot Jupiter that could be incorporated in traditional GCMs.

6. Discussion and conclusion

6.1. Main results

Using a series of high resolution idealized simulations of hot–Jupiters atmospheres that solve the Euler equations with a finite volume shock-capturing scheme, we have found the following results:

- Numerical simulations performed in the framework of the equatorial β–plane model are in good agreement with results published in the literature using a wide range of models and elaborate treatments of the radiative effects.
- A supersonic, equatorial, eastward jet forms quickly in the upper layers of the atmosphere. At $P \sim 50$ mbars, its zonally averaged velocity reaches about ~ 7 km.s^{-1} and is found to be sensitive to the meridional resolution (or, equivalently, to the dissipation).
- At large enough spatial resolution (or low enough dissipation), the jet displays large velocity fluctuations that can be attributed to meanders upward of ~ 1 bars and smaller scale fluctuations with an amplitude of a few tens of m.s^{-1} at pressure levels $P \sim 1$–10 bars.
- The meanders are clearly associated with a barotropic Kelvin-Helmholtz instability that results in quasi–periodic modulations of the jet velocity with a typical period of ~ 10 days. The properties of the flow are broadly consistent with the expectations of linear stability analysis. Temperature fluctuations of a few hundred Kelvins are found at the photosphere of the planet at the peak of the instability, most likely a result of adiabatic compression associated with the equatorial jet meanders. Future work is needed to determine whether these variations are compatible with the observed upper limit of 2.7% of the dayside variability of HD189733b (Agol et al. 2010; Knutson et al. 2012) and whether they could be observable with the JWST using brightness mapping such as discussed by de Wit et al. (2012).
- The smaller scales fluctuations are likely associated with a vertical shear instability. They correlate nicely with the locations where the Richardson number is smaller than 1/4. They create zonal variations of the jet velocity with a spatial scale of $\sim 10^4$ km that is consistent with the most unstable mode predicted by a linear analysis (Li & Goodman 2010).
- The dissipation of the kinetic energy associated to the vertical shear instability results in a substantial increase of the temperature at $P \sim 10$ bars. This thus confirms that the atmosphere converts stellar energy into kinetic energy that is transported downward to be deposited at deeper levels (Showman & Guillot 2002). A better treatment of the lower boundary is needed to know whether the deposition level can be deep enough to affect the interior and help explain the radius anomaly (Guillot & Showman 2002).
- We find weak shocks in the upper layers of the atmosphere ($P < 10$ mbars). They have typical upstream Mach numbers between 1 and 2 and create temperature fluctuations of a few hundreds Kelvins. At larger pressure ($P > 10$ mbars), we find no shocks despite the supersonic nature of the equatorial jet.

6.2. Limitations and future work

These results should not hide the limitations of the work presented here that are as many avenues for progress. As noted in section 2, the model depends on a number of free parameters. The motivation of the present paper was to choose a unique set of these parameters so that the flow properties matches that of the benchmark calculation described by Heng et al. (2011b). Even if the dynamical mechanisms responsible for the instabilities highlighted here are fairly general, future work is needed to investigate systematically the sensitivity of the results presented here to each of these parameters and to make quantitative predictions that would be valuable for more realistic atmospheres. For example, we note that the zonal wind velocity we obtained tends to be larger than commonly found by other authors. Is it because we work in the framework of the equatorial β–plane model? Or is it related to the form of the thermal forcing we use, and in particular to the value of L_{th}? Another question is that of convergence with spatial resolution: it is possible (and even likely!) that numerical dissipation is still affecting the instabilities described in section 5.1 and 5.2. This may affect their saturation properties and their quantitave effect of the mean flow, and particularly on the velocity of the jet. The present work shows that a proper convergence study (systematically varying both the meridional and the vertical resolution)—even though it is very computationally demanding—is definitely needed.

Perhaps the most stringent limitation of the present work comes from the presence of an "inert" layer below 10 bars where the radiative timescale τ_{rad} goes to infinity. The large temperature increase we see at this location is probably overestimated because of the inability of the gas to cool radiatively. This problem may be somewhat mitigated upon noting that τ_{rad} is expected to increase rapidly in the deep layers of hot Jupiters atmospheres ($P \leq 10$–100 bars). For example, Showman et al. (2008) use $\tau_{rad} = 10^8$ seconds at 20 bars. This is more than 300 planet days and much faster than the timescale of a few days that is associated with the vertical shear instability (see fig. 15), so that the effect of choosing an infinite value for τ_{rad} may not be as severe as naively expected. Nevertheless, it is clear that a large temperature increase such as found here acts as a positive feedback onto the vertical shear instability by reducing the Richardson number Ri. Whether or not it affects the findings presented in this paper, and how much, remains to be clarified. One possibility to do so is to replace the Newtonian relaxation scheme with a simplified radiative transfer scheme (Heng et al. 2011a; Rauscher & Menou 2012). This may alleviate that problem in the deep atmosphere.

The need to strengthen these results is made even more important because standard GCM codes that use the primitive formulation of the hydrodynamic equations are unable to account for such vertical shear instabilities. By assuming hydrostatic equilibrium in the vertical direction, they assume *de facto* that such an instability does not exist. Instead, they rely on subgrid scale modelling to include their effect on the flow. Future work is therefore needed to validate these subgrid models and/or develop more appropriate approaches if necessary. This is an important step to validate the long–term use of such codes as the primary tool to model hot Jupiter atmospheric flows.

Appendix A: Equilibrium temperature and cooling timescale

We give here for reference the pressure profiles of T_P^0 and τ_{rad} that we have used in this paper. They are a simplified version of the profiles presented by Heng et al. (2011b). The thermal timescale τ_{rad} is calculated with the following relation:

$$\tau_{rad} = \begin{cases} \tau_0 \, (P_0/P)^{\alpha_0} & \text{if } P < P_0 \\ \tau_1 \, (P_1/P)^{\alpha_1} & \text{if } P_0 < P < P_1 \\ +\infty & \text{if } P > P1 \end{cases} , \qquad \text{(A.1)}$$

where $P_0 = 1$ bar, $P_1 = 10$ bars, $\tau_0 = 10^5$ and $\tau_1 = 10^{7.5}$ seconds. The dimensionless exponent α_0 and α_1 respectively

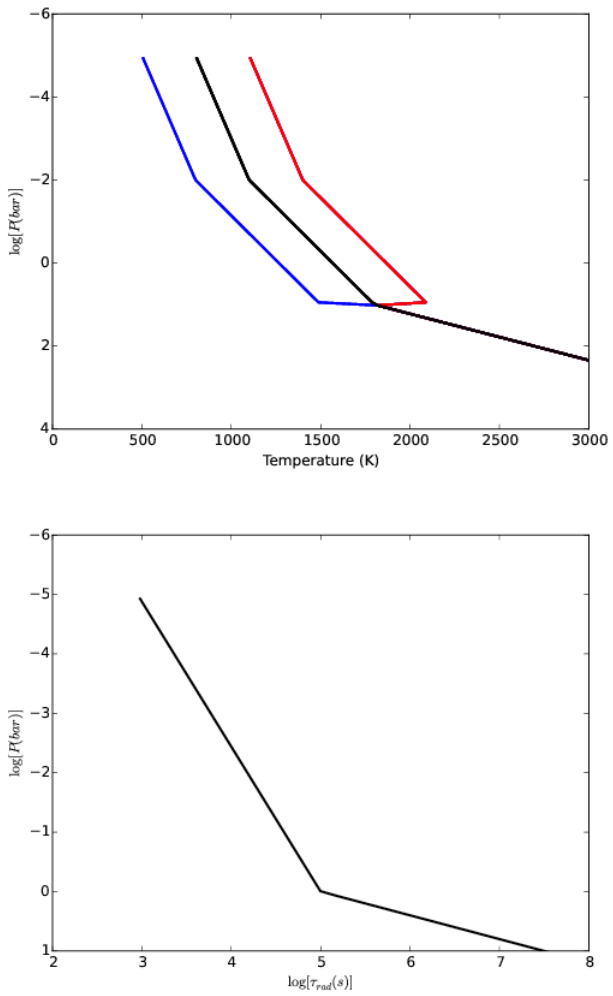

Fig. A.1: Pressure variations of the equilibrium temperature T_{eq} (*top panel*) and the Newtonian relaxation time τ_{rad} (*bottom panel*) used to calculate the cooling function $\mathcal{L}$ in the deep hot Jupiter model presented in this paper.

amounts to −0.41 and −2.5. Likewise, T_P^0 is given as a combination of linear functions of the logarithm of the pressure:

$$T_{iro} = \begin{cases} T_{-2} - \gamma_{-2} \log(P_{-2}/P) & \text{if } P < P_{-2} \\ T_1 - \gamma_1 \log(P_1/P) & \text{if } P_{-2} < P < P_1 \\ T_2 - \gamma_2 (P_2/P) & \text{if } P > P1 \end{cases}, \quad \text{(A.2)}$$

where $P_{-2} = 10^{-2}$ bar and T_{-2}, T_1 and T_2 are respectively set to 1100, 1800 and 3000 K. The slopes of the linear relations are given by $\gamma_{-2} = 100$ K, $\gamma_1 = 233$ K and $\gamma_2 = 983$ K. The relation between τ_{rad} and P and between T_P^0 and P are shown in figure A.1 where we also display the variation of T_{day} and T_{night} such as defined in section 2.2. All curves are meant to be compared with, for example, figure 7 of Heng et al. (2011b) with which they are in good agreement.

Appendix B: Numerical tests

B.1. Baroclinic instability in an adiabatic atmosphere

As argued by Polichtchouk et al. (2014), the growth of a baroclinic wave is a severe test for codes that pretend to describe

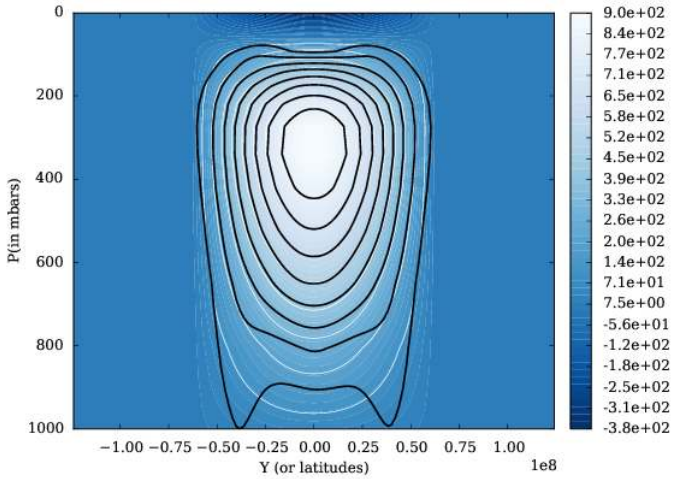

Fig. B.1: Initial (i.e. at $t = 0$) zonally averaged zonal wind used for the baroclinic instability simulations (colors and white contours). The black contour show the zonally averaged zonal wind at the end of the simulation for the model with resolution $(N_x, N_y, N_z) = (256, 128, 32)$. Contours are drawn every 100 m.s^{-1} from 100 to 900 m.s^{-1}.

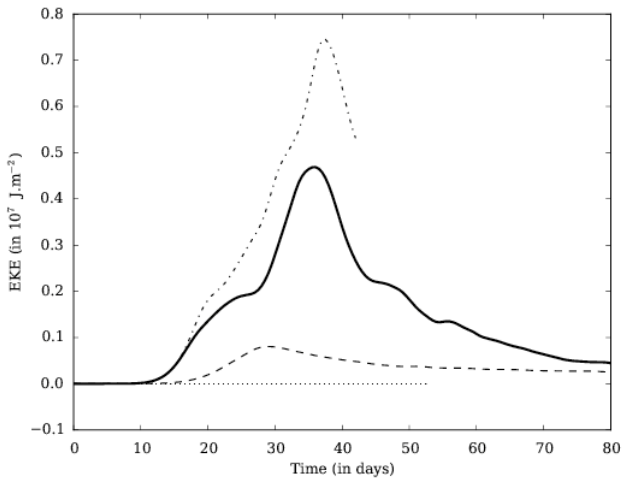

Fig. B.2: Time evolution of the volume integrated eddy kinetic energy (per unit area) in the baroclinic instability test. The solid and dotted lines both share the resolution $(N_x, N_y, N_z) = (256, 128, 32)$ and corresponds to the model with and without an initial temperature perturbation, respectively. The dashed and dotted–dashed lines shows the results of the models with resolution $(N_x, N_y, N_z) = (128, 64, 32)$ and $(N_x, N_y, N_z) = (512, 256, 32)$, respectively.

accurately atmospheric flows because it grows slowly from infinitesimal perturbations. This is even more so for finite volume codes such as RAMSES that have problems handling hydrostatic equilibria, and we found that problem to be very helpful in assessing the robustness of our setup. In this appendix, we thus qualitatively reproduce one of the model presented by Polichtchouk & Cho (2012), namely their equatorial jet case, since the base flow is close to the jet configuration studied in the present paper. As noted by Polichtchouk et al. (2014), the detailed evolution of the atmosphere is very sensitive to the exact

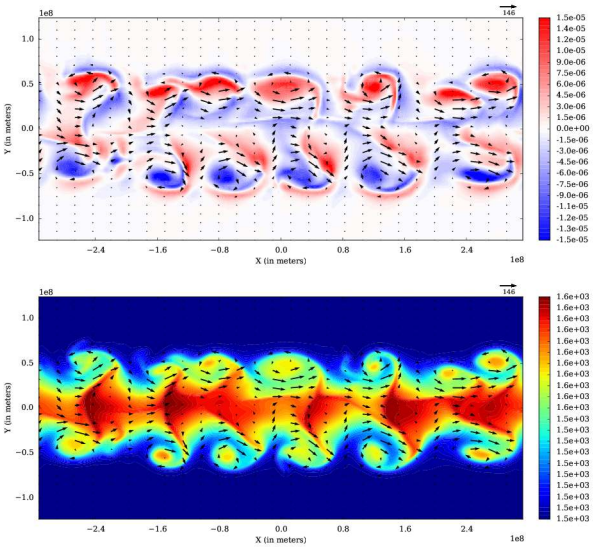

Fig. B.3: Relative vorticity (*top panel*) and temperature (*bottom panel*) distribution in the horizontal plane at 930 mbars, at time $t = 32$ showing the development of a baroclinic wave that grows on top of a zonal equatorial jet. The parameters are chosen after Polichtchouk & Cho (2012) and the resolution is $(N_x, N_y, N_z) = (256, 128, 32)$.

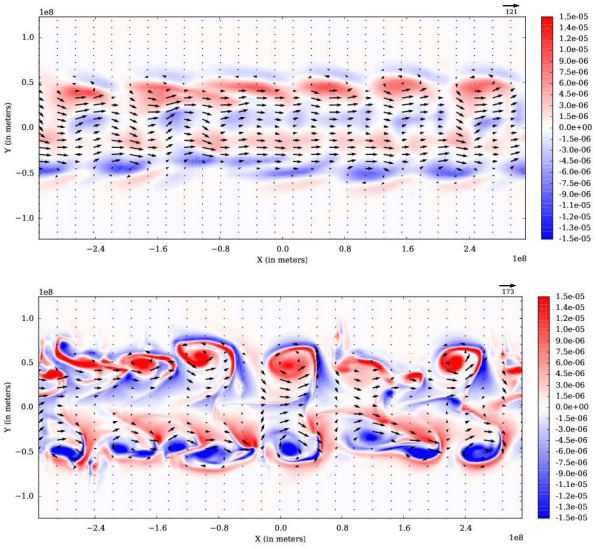

Fig. B.4: Relative vorticity at 930 mbars at time $t = 32$ for the baroclinic instability growth with resolution $(N_x, N_y) = (128, 64)$ (*top panel*) and $(N_x, N_y) = (512, 128)$ (*bottom panel*).

structure of the jet and the initial perturbation, so that our goal here is not to reproduce quantitatively the results of Polichtchouk & Cho (2012), but rather to show that we obtain the same qualitative evolution of the flow. Indeed, since we neither use the same equations (Euler vs. primitive) nor the same geometry (cartesian vs. spherical), a one to one quantitative comparison is not possible.

The structure of the atmosphere at $t = 0$ is computed assuming thermal wind balance after having specified the jet zonal velocity. The latter is computed using the following relation, adapted to the equatorial β–plane geometry from Polichtchouk & Cho (2012):

$$u(x,y) = \begin{cases} U_0 G(z) \sqrt{\sin\left[\pi \sin^2\left(\frac{\pi}{2}\frac{4y+L_y}{2L_y}\right)\right]}, & |y| < L_y/4 \\ 0\,, & \text{otherwise} \end{cases}$$

where G is defined as:

$$G(z) = \frac{1}{2}\left[1 - \tanh^3\left(\frac{z - z_J}{\Delta z_J}\right)\right] \sin\left(\pi \frac{z}{L_z}\right).$$

The previous relations depend on a number of free parameters. In this appendix, we use $z_J = 0.8 L_z$, $\Delta z_J = 0.2 L_z$, $U_0 = 1000$ m.s^{-1} and $L_z = 2 \times 10^6$ m.s^{-1}. The initial structure of the jet is shown on figure B.1 and resembles that shown on their figure 4 (right panel) by Polichtchouk & Cho (2012) . Next, a localized temperature perturbation of amplitude δT_0 is added at all pressure levels in the atmosphere. It takes the form:

$$\delta T(x,y) = \delta T_0 \,\mathrm{sech}^2\left(\frac{6\pi x}{L_x}\right) \mathrm{sech}^2\left(\frac{\pi}{3}\frac{4y - L_y}{2L_y}\right), \qquad \text{(B.1)}$$

so that it is localized initially at $x = 0$ and $y = L_y/4$, i.e. on the jet northern flank.

We first present and contrast the results of two simulations with resolution $(N_x, N_y, N_z) = (256, 128, 32)$ and for which we respectively set $\delta T_0 = 0$ (control run) and 1 K (perturbed run). We computed the volume integral of the specific eddy kinetic energy (EKE) as a diagnostic of the baroclinic instability growth:

$$EKE = \int_V \rho \left[u'^2 + v'^2\right] dV\,. \qquad \text{(B.2)}$$

As described by Polichtchouk & Cho (2012), the specific EKE grows after a few days in the perturbed case (see figure B.2) as a result of a baroclinic wave but stays very small in the control run during the entire simulation. In fact, the specific EKE remains at the level of 10^{-10} J/m^{-2} (i.e. 17 orders of magnitude smaller than the perturbed model after the growth of the baroclinic wave!), indicating that our numerical scheme accurately conserves the symmetry of the flow and the initial atmospheric hydrostatic equilibrium (the maximum meridional velocity at the end of that run at 975 mbars is only of the order of 8 cm.s^{-1}!). In the perturbed run, the specific EKE peaks between $t = 30$ and $t = 35$. The flow at 975 mbars shows five well defined cyclones that roll on both sides of the jet (see figure B.3), clearly correlated with temperature fluctuations. This is again in very good qualitative agreement with the results of Polichtchouk & Cho (2012). We note that the number of cyclones and the amplitude of the vorticity perturbations they display is also in good quantitative agreement with those results. Finally, after a few tens of days, the specific EKE saturates and decays. At the end of the model evolution, the equatorial jet structure is modified and displays a vertical structure that is more barotropic (see figure B.1, black contours), in agreement with the finding of Polichtchouk & Cho (2012).

We have also performed a resolution study, keeping the number of vertical levels fixed to $N_z = 32$, and gradually varying the horizontal resolution from $(N_x, N_y) = (128, 64)$ to $(N_x, N_y) = (512, 256)$, although the highest resolution simulation is only integrated to $t = 45$. The vorticity distribution at 975 mbars (see figure B.4) shows that the minimum resolution required to capture the instability is $(N_x, N_y) = (256, 128)$ and that the structure of the flow is qualitatively captured at that resolution, although quantitatively, figure B.2 shows that the growth rate is not converged yet. This resolution study gives a useful comparison with

Parameters	Symbol	Value
Box vertical size (m)	L_z	3×10^6
Pressure at bottom boundary (Pa)	P_0	10^5
Day-night temperature difference (K)	ΔT	300
Cooling time scale (sec)	τ_{rad}	1.5×10^5
Cut–off length of cooling function (m)	L_{th}	3.5×10^7
Temperature at bottom boundary (K)	$T_{\rm surf}$	1600
Tropospheric lapse rate (K.m^{-1})	$\Gamma_{\rm trop}$	2×10^{-4}
Tropopause temperature increment (K)	$\delta T_{\rm stra}$	10
Tropopause pressure (Pa)	$\sigma_{\rm stra}$	1.25×10^4

Table B.1: Parameters used for the shallow hot Jupiter model.

the analysis of Polichtchouk & Cho (2012) who used a spectral numerical scheme and somewhat mitigate their claim that finite difference shemes require resolution larger by an order of magnitude to capture the growth of the baroclinic wave. Here, it appears that a difference of about a factor of two is sufficient.

Overall, the results presented here are in good qualitative agreement with the results of Polichtchouk & Cho (2012) and Polichtchouk et al. (2014) and give credit to our implemantation.

B.2. A shallow hot Jupiter model

We next reproduce the benchmark simulation of a shallow hot Jupiter, such as presented by Menou & Rauscher (2009), Heng et al. (2011b), Bending et al. (2013) and Mayne et al. (2014a). As for the case of the baroclinic instability presented above, we have adapted the setup described by these authors to the equatorial β–plane. It differs from the deep hot Jupiter model by the depth of the atmosphere, which extends downward only to 1 bar, and by the parameters entering in the cooling function $\mathcal{L}$. More specifically, τ_{rad} is a constant equal to half a planet day and T_{eq} is given by the function:

$$T_{eq} = T_{perp} + \beta_{\rm trop} \Delta T \cos\left(\frac{2\pi x}{L_x}\right) \exp\left(-\frac{y^2}{2L_{th}^2}\right), \qquad \text{(B.3)}$$

where T_{perp} and $\beta_{\rm trop}$ depend on z according to

$$T_{perp} = T_{\rm surf} - \Gamma_{\rm trop}\left(z_{\rm stra} + \frac{z - z_{\rm stra}}{2}\right) + \sqrt{\delta T_{\rm stra}^2 + \left(\frac{\Gamma_{\rm trop}}{2}[z - z_{\rm stra}]\right)^2} \qquad \text{(B.4)}$$

and

$$\beta_{\rm trop} = \begin{cases} \sin\left(\frac{\pi}{2}\frac{\sigma - \sigma_{\rm stra}}{1 - \sigma_{\rm stra}}\right), & \text{if } z < z_{\rm stra} \\ 0, & \text{otherwise.} \end{cases} \qquad \text{(B.5)}$$

The different parameters of the problem are taken identical to the original papers mentioned above and are recalled for completness in table B.1. In our case, we also need to specify the location of the upper boundary of the domain, which we take to be $L_z = 3 \times 10^6$ meters, while we retain for L_x and L_y the same values as for the deep model described in section 2.4. L_{th} and β also take values identical to those of the main body of the paper. We start our simulation with an atmosphere initially at rest and in hydrostatic equilibrium with $T = T_{\rm perp}$. We integrate the hydrodynamics equations for 300 planet days, of which the last 200 days are used to produce time averaged fields. The grid resolution is chosen to be $(N_x, N_y, Nz) = (64, 32, 24)$.

As for the deep hot Jupiter model described in section 3, we find that a fast equatorial wind develops with typical amplitude

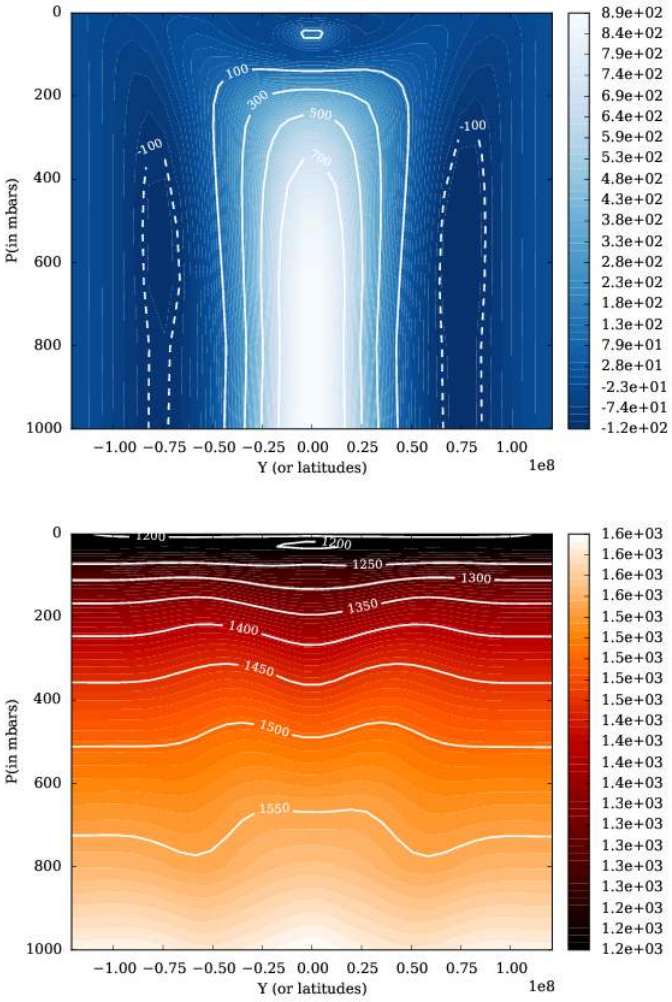

Fig. B.5: Zonally averaged zonal wind (*top panel*) and temperature (*bottom panel*) in the shallow hot Jupiter model. The raw simulation data are averaged over 200 planet days starting at $t = 100$. See text and table B.1 for the model parameters.

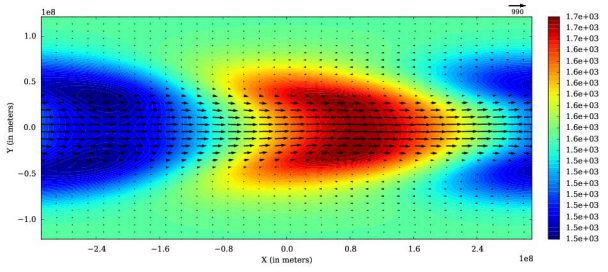

Fig. B.6: Temperature (*color contours*) and wind velocities at the 750 mbars pressure level in the shallow hot Jupiter model, averaged in time over 200 planet days starting at $t = 100$.

of 1000 m.s^{-1}. Here, however, the flow display significant fluctuations with typical wind velocity fluctuations of a few tens of m.s^{-1} (not shown). These fluctuations have also been reported by previous authors and likely result from the interaction between the atmosphere and the bottom domain boundary. The time averaged spatial distributions of the zonally averaged zonal wind and temperature are both in good agreement with the papers men-

tionned above (see figure B.5). Likewise, the temperature distribution at 750 mbars display the familiar chevron–like shape that has been identified as the consequence of planetary scale waves by Showman & Polvani (2010, 2011).

The good agreement of our results with previously published simulations of shallow hot Jupiter atmospheres demonstrate that the equatorial β plane model is appropriate for the study of slowly rotating tidally locked gas giant planet.

ACKNOWLEDGMENTS

SF research is funded by the European Research Council under the European Union's Seventh Framework Programme (FP7/2007-2013) / ERC Grant agreement n 258729. SF acknowledges the hospitality of the Kavli Institute of for Theoretical Physics, Santa Barbara, where some of this work was completed during the program "Wave–flow interaction in Geophysics, climate, astrophysics and plasmas" as well as enlightening discussions with Gwendal Rivière.

References

Agol, E., Cowan, N. B., Knutson, H. A., et al. 2010, ApJ, 721, 1861
Baraffe, I., Chabrier, G., & Barman, T. 2010, Reports on Progress in Physics, 73, 016901
Bending, V. L., Lewis, S. R., & Kolb, U. 2013, MNRAS, 428, 2874
Cho, J. Y.-K., Menou, K., Hansen, B. M. S., & Seager, S. 2008, ApJ, 675, 817
Cho, J. Y.-K., Polichtchouk, I., & Thrastarson, H. T. 2015, ArXiv e-prints
de Wit, J., Gillon, M., Demory, B.-O., & Seager, S. 2012, A&A, 548, A128
Dobbs-Dixon, I., Cumming, A., & Lin, D. N. C. 2010, ApJ, 710, 1395
Dobbs-Dixon, I. & Lin, D. N. C. 2008, ApJ, 673, 513
Drazin, P. G. & Reid, W. H. 1981, NASA STI/Recon Technical Report A, 82
Ginzburg, S. & Sari, R. 2015, ApJ, 803, 111
Goodman, J. 2009, ApJ, 693, 1645
Guillot, T. & Showman, A. P. 2002, A&A, 385, 156
Heng, K. 2012, ApJ, 761, L1
Heng, K., Frierson, D. M. W., & Phillipps, P. J. 2011a, MNRAS, 418, 2669
Heng, K., Menou, K., & Phillipps, P. J. 2011b, MNRAS, 413, 2380
Heng, K. & Showman, A. P. 2015, Annual Review of Earth and Planetary Sciences, 43, 509
Heng, K. & Workman, J. 2014, ApJS, 213, 27
Käppeli, R. & Mishra, S. 2014, Journal of Computational Physics, 259, 199
Knutson, H. A., Charbonneau, D., Allen, L. E., et al. 2007, Nature, 447, 183
Knutson, H. A., Lewis, N., Fortney, J. J., et al. 2012, ApJ, 754, 22
LeVeque, R. J. 1998, Journal of Computational Physics, 146, 346
Li, J. & Goodman, J. 2010, ApJ, 725, 1146
Liu, B. & Showman, A. P. 2013, ApJ, 770, 42
Madhusudhan, N., Knutson, H., Fortney, J. J., & Barman, T. 2014, Protostars and Planets VI, 739
Mayne, N. J., Baraffe, I., Acreman, D. M., et al. 2014a, A&A, 561, A1
Mayne, N. J., Baraffe, I., Acreman, D. M., et al. 2014b, Geoscientific Model Development, 7, 3059
Menou, K., Cho, J. Y.-K., Seager, S., & Hansen, B. M. S. 2003, ApJ, 587, L113
Menou, K. & Rauscher, E. 2009, ApJ, 700, 887
Perez-Becker, D. & Showman, A. P. 2013, ApJ, 776, 134
Polichtchouk, I. & Cho, J. Y.-K. 2012, MNRAS, 424, 1307
Polichtchouk, I., Cho, J. Y.-K., Watkins, C., et al. 2014, Icarus, 229, 355
Rauscher, E. & Menou, K. 2010, ApJ, 714, 1334
Rauscher, E. & Menou, K. 2012, ApJ, 750, 96
Showman, A. P., Cooper, C. S., Fortney, J. J., & Marley, M. S. 2008, ApJ, 682, 559
Showman, A. P., Fortney, J. J., Lian, Y., et al. 2009, ApJ, 699, 564
Showman, A. P. & Guillot, T. 2002, A&A, 385, 166
Showman, A. P. & Polvani, L. M. 2010, Geophys. Res. Lett., 37, 18811
Showman, A. P. & Polvani, L. M. 2011, ApJ, 738, 71
Snellen, I. A. G., de Kok, R. J., de Mooij, E. J. W., & Albrecht, S. 2010, Nature, 465, 1049
Teyssier, R. 2002, A&A, 385, 337
Thrastarson, H. T. & Cho, J. Y. 2010, ApJ, 716, 144
Toro, E. 1997, Riemann solvers and numerical methods for fluid dynamics (Springer)
Tsai, S.-M., Dobbs-Dixon, I., & Gu, P.-G. 2014, ApJ, 793, 141
Vallis, G. K. 2006, Atmospheric and Oceanic Fluid Dynamics
Watkins, C. & Cho, J. Y.-K. 2010, ApJ, 714, 904
Youdin, A. N. & Mitchell, J. L. 2010, ApJ, 721, 1113
Zhu, Z., Stone, J. M., & Rafikov, R. R. 2013, ApJ, 768, 143